

# Testing *WMAP* data via *Planck* radio and SZ catalogues

J.R. Whitbourn<sup>1</sup>\*, T. Shanks<sup>1</sup> and U. Sawangwit<sup>1,2</sup>

<sup>1</sup>*Department of Physics, Durham University, South Road DH1 3LE*

<sup>2</sup>*National Astronomical Research Institute of Thailand, Thailand*

Accepted ; Received ; in original form

## ABSTRACT

The prime evidence underpinning the standard  $\Lambda$ CDM cosmological model is the CMB power spectrum as observed by *WMAP* and other microwave experiments. But Sawangwit & Shanks (2010a) have recently shown that the *WMAP* CMB power spectrum is highly sensitive to the beam profile of the *WMAP* telescope. Here, we use the source catalogue from the *Planck* Early Data Release to test further the *WMAP* beam profiles. We confirm that stacked beam profiles at Q, V and particularly at W appear wider than expected when compared to the Jupiter beam, normalised either directly to the radio source profiles or using *Planck* fluxes. The same result is also found based on *WMAP*-CMBfree source catalogues and NVSS sources. The accuracy of our beam profile measurements is supported by analysis of CMB sky simulations. However the beam profiles from *WMAP7* at the W band are narrower than previously found in *WMAP5* data and the rejection of the *WMAP* beam is now only at the  $\approx 3\sigma$  level. We also find that the *WMAP* source fluxes demonstrate possible non-linearity with *Planck* fluxes. But including ground-based and *Planck* data for the bright Weiland et al. (2011) sources may suggest that the discrepancy is a linear offset rather than a non-linearity. Additionally, we find that the stacked Sunyaev-Zel'dovich (SZ) decrements of  $\approx 151$  galaxy clusters observed by *Planck* are in agreement with the *WMAP* data. We find that there is no evidence for a *WMAP* SZ deficit as has previously been reported. In the particular case of Coma we find evidence for the presence of an  $\mathcal{O}(0.1mK)$  downwards CMB fluctuation. We conclude that beam profile systematics can have significant effects on both the amplitude and position of the acoustic peaks, with potentially important implications for cosmology parameter fitting.

**Key words:** cosmology: cosmic microwave background - large-scale structure of Universe

## 1 INTRODUCTION

Cosmic Microwave Background (CMB) experiments such as the Wilkinson Microwave Anisotropy Probe (*WMAP*) have made significant progress in the study of the primordial temperature fluctuations. Their best fitting power spectra strongly support a spatially flat,  $\Lambda$ CDM, universe. This model requires relatively few parameters, yet apparently manages a compelling concordance between a variety of other cosmological data; SNIa, Large Scale Structure and Big Bang Nucleosynthesis. Although the statistical errors on these power spectra are small, this precision does not necessarily imply accuracy and there remains the potential for systematic errors to alter these conclusions.

Indeed, several anomalies between  $\Lambda$ CDM and the

*WMAP* data have been discussed. Typically these have involved the large-scale temperature multipoles eg: (Bennett et al. 2011; Liu & Li 2011). However, other anomalies in the CMB at smaller scales have also been detected, connected in particular with radio sources (Sawangwit & Shanks 2010a,b) and SZ decrements from galaxy clusters (Myers et al. 2004; Bielby & Shanks 2007)

Radio sources are sometimes regarded as a contaminant in CMB temperature maps. However, radio point sources prove particularly interesting because they provide a complementary check of the beam measured by the *WMAP* team from observations of Jupiter (Page et al. 2003; Hill et al. 2009). Jupiter has a flux of  $\approx 1200$ Jy which is  $\approx 3$  orders of magnitude higher than radio source fluxes or CMB fluctuations. This high flux has advantages in terms of defining the wings of the beam profile but has the disadvantage that the calibrating source is much brighter than

\* Corresponding author:(JRW) joseph.whitbourn@durham.ac.uk

typical CMB fluctuations. Furthermore, Jupiter only checks the beam on the ecliptic whereas radio sources are spread over the sky. Sawangwit & Shanks (2010a,b) made a stacked analysis of radio point sources and found evidence for a wider beam than *WMAP* measured using Jupiter. A tentative detection of a non-linear relation between *WMAP* fluxes and ground based radio telescope fluxes was also found. A thorough analysis of possible systematics did not find an explanation and we return to these issues later in this paper. The beam profile of a CMB telescope like *WMAP* is critical because it smooths the temperature anisotropies and therefore needs to be known accurately to produce the final power spectrum from temperature maps (Page et al. 2003; Hill et al. 2009).

Various authors have noted small-scale anomalies with respect to the SZ decrements measured by *WMAP*. SZ decrements are created when CMB photons inverse Compton scatter off hot electrons in galaxy clusters. Myers et al. (2004) first stacked *WMAP* data at the positions of galaxy clusters and suggested that the profiles were more extended than expected. Lieu, Mittaz, & Zhang (2006) and Bielby & Shanks (2007) then found that the SZ decrements from *WMAP* were reduced compared to X-ray predictions, possibly due to the *WMAP* beam being wider than expected. Bielby & Shanks (2007) also found that the *WMAP* decrements were significantly lower than the ground-based SZ measurements by Bonamente et al. (2006) in 38 X-ray luminous clusters.

In their ESZ sample, the *Planck* team find excellent agreement with the self-similar X-ray estimates of the SZ decrement (*Planck* Collaboration et al. 2011f,g). This is corroborated by the ground based South Pole Telescope Collaboration with their blind SZ selected cluster sample (Mroczkowski et al. 2009). This compounds the question of why *WMAP* SZ analyses from Lieu, Mittaz, & Zhang (2006) and Bielby & Shanks (2007) failed to find such an agreement.

In this paper we use the recent *Planck* Early Data Release and other radio source data to re-investigate both the *WMAP* radio source beam profile and SZ anomalies. The *Planck* Early Release Compact Source catalogue (ERCSC) is of particular interest and provides the basic parameters of radio sources and SZ clusters from the *Planck* CMB maps. Although, the corresponding temperature maps from which these were estimated have not been released, both radio source fluxes and SZ profile parameters are available as measured by *Planck*. We can therefore use these to compare *WMAP* and *Planck* radio source fluxes directly and also to make *WMAP* stacks centred now on the new radio source and SZ cluster lists from *Planck*. From these stacks, the *WMAP* beam profile can be inferred and the SZ results from *WMAP* and *Planck* compared. Given the higher angular resolution, lower noise and different calibration strategy for *Planck*, this comparison will allow new insight into the robustness of the *WMAP* CMB analysis.

## 2 DATA

### 2.1 *Planck* Early Data Release

The *Planck* team have recently made their first release of data collected by the *Planck* satellite between 13 August

2009 and 6 June 2010 (amounting to  $\approx 1.5$  full sky surveys). This early data release is concerned solely with the foreground contamination in the CMB maps. The two sets of catalogues relevant to this paper form the Early Release Compact Source catalogue (ERCSC). These are the Radio Source catalogues and the SZ catalogue.

#### 2.1.1 *Planck* Radio Sources

The Early Release Compact Source Catalogue (ERCSC) lists all the high reliability radio sources with accurate flux determinations. The ERCSC has been quality controlled so that  $\geq 90\%$  of the reported sources are reliable,  $> 5\sigma$ , detections and that the fluxes are determined within  $\leq 30\%$  accuracy. The catalogues are band specific and for the bands of interest ( $\nu \leq 100\text{GHz}$ ) are created using the ‘PowellSnakes’ method, a Bayesian multi-frequency algorithm for detecting discrete objects in a random background. Flux estimates were obtained by use of aperture photometry within a circle of the beam’s FWHM. For the case of unresolved and potentially faint point sources, the *Planck* team recommend the use of the parameter FLUX and its corresponding error, FLUX\_ERR (*Planck* Collaboration et al. 2011exp).

We reject any extended objects from the catalogue to maintain an unresolved sample with which to test the *WMAP* data. To do this we have used the *Planck* quality tag ‘EXTENDED’. This is defined by comparing the source areal profile with the 2-D *Planck* beam. An additional quality flag ‘CMBSUBTRACT’ has also been provided, which reflects on the quality of the source detection in a map with the best estimate of the CMB removed. We minimise CMB contamination by using only CMBSUBTRACT=0 sources.

When measuring the beam profile in Section 6 we further cut the catalogue to ensure the best quality sample. Sawangwit & Shanks (2010a) did suggest that their faintest *WMAP* source samples were probably affected by Eddington (1913) bias. To ensure the robustness of our results against Eddington bias, we have used a  $S \geq 1.1\text{Jy}$  flux cut, the same limit as previously used by Sawangwit & Shanks (2010a). We have additionally rejected sources within  $4^\circ$  of the LMC, sources at low galactic latitude,  $|b| < 5^\circ$  and any sources flagged by *Planck* as having high astrometric error. Finally, we tightened the *Planck* ‘EXTENDED’ flag to remove any sources intrinsically wider than the *WMAP* beam. The *Planck* ‘EXTENDED’ flag excludes sources with  $(GAU_{FWHM\_MAJ} \times GAU_{FWHM\_MIN})^{1/2} > 1.5 \times (BEAM_{FWHM\_MAJ} \times BEAM_{FWHM\_MIN})^{1/2}$ . We now ensure that the *Planck* sources are unresolved in the *WMAP* maps by imposing cuts in both the major and minor axis so that both the fitted Gaussian profiles (GAU) and the local PSF (BEAM) FWHM estimates are less than the FWHM of the *WMAP* beam in the band being studied<sup>1</sup>.

Band and colour corrections for the *WMAP* and *Planck* fluxes have been ignored. This factor is in any case small due to the typically flat spectral indices considered (*Planck* Collaboration et al. 2011exp; Wright et al. 2009).

<sup>1</sup> We relax this cut for the Q-band, here we only impose cuts on local PSF (BEAM) FWHM estimates to ensure we get a reasonable number of sources.

The full details of the catalogue construction and composition are described by *Planck* Collaboration et al. (2011d) and briefly overviewed in Table 2.2.

### 2.1.2 Planck SZ Catalogue

The Early SZ (ESZ) catalogue lists all the robust and extensively verified SZ detections in the first data release. As described by Melin, Bartlett, & Delabrouille (2006), the *Planck* team extract the integrated SZ signal, the  $Y$  parameter, using a Multifrequency Matched filter (MMF3) method (*Planck* Collaboration et al. 2011d). The algorithm is run blindly on all-sky maps, assuming the characteristic SZ spectral signature and self-similar cluster profile.

In the Early Release of the *Planck* SZ catalogue, only data from the 100GHz frequency channel or higher has been used to study the SZ effect. This is to avoid the detrimental effect on S/N from beam dilution caused by the larger beam sizes of the lower frequency channels. At the higher frequencies, the *Planck* beam FWHM is typically  $\approx 4.5'$ . The full details of the catalogue construction and composition are described by the *Planck* Collaboration et al. (2011d).

The catalogue provides estimates of the SZ flux, extent, redshift and position. It consists of 189 clusters, all detected at high S/N ( $\geq 6$ ) with 95% reliability. Whilst the sample is primarily composed of known clusters (169/189), it provides a wealth of new information as it gives the first SZ measurements for  $\approx 80\%$  of the clusters. In this paper we only make use of clusters which have been pre-detected in the X-ray and have redshifts. We therefore, after masking, consider 151 clusters, including Coma. For this sample the redshift range spans  $z \in [0.0126, 0.546]$  with a mean redshift of  $\bar{z} = 0.18$ .

## 2.2 WMAP Data

We will be using the 7-year *WMAP* temperature maps obtained from the LAMBDA CMB resource. We work with the  $N_{side} = 512$  HEALPIX maps resulting in a pixel scale of  $7'$ . We use the foreground unsubtracted temperature band maps for Q, V and W. Our default *WMAP* datasets are the co-added maps in Q (=Q1+Q2), V (=V1+V2) and W (=W1+W2+W3+W4). However, particularly in the W band, the increased S/N for radio source profiles obtained by using all the DA's can be regarded as a trade-off with the precision of just using the narrowest W1 (and W4) beams as previously used by Sawangwit & Shanks (2010a). In using the co-added data, the Jupiter beams have to be combined before comparison with the data. We estimate the Jupiter beam in each band by averaging the 7-year beam profiles from the various detector assemblies, assuming the appropriate correction for pixelisation (Hinshaw et al. 2003). When working with radio point sources we use the point source catalogue mask (`wmap_point_source_catalog_mask`). To avoid Galactic contamination for the SZ analyses we have instead used the extended temperature mask (`wmap_ext_temperature_analysis_mask`) which admits 71% of the sky.

We have used the 7-year *WMAP* 5-band point source catalogue (Gold et al. 2011). These sources are detected at least the  $5\sigma$  level in one *WMAP* band. For a flux density

Freq [GHz]	FWHM (')	Flux Limit [Jy]
100	9.94	0.344
70	13.01	0.481
44	27.00	0.781

**Table 1.** Summary of the *Planck* bandpass parameters and the flux range of the sample we use from the ERCSC, (*Planck* Collaboration et al. 2011exp).

Band	Freq [GHz]	FWHM (')	$\Omega$ (sr)	$\Gamma^{ff}$ [ $\mu K Jy^{-1}$ ]	$g(\nu)$
W	94	12.6	$2.097 \cdot 10^{-5}$	179.3	1.245
V	61	19.8	$4.202 \cdot 10^{-5}$	208.6	1.099
Q	41	29.4	$8.978 \cdot 10^{-5}$	216.6	1.044

**Table 2.** Summary of the *WMAP* bandpass parameters taken from Hill et al. (2009) and Jarosik et al. (2011). See text for definitions.

to be stated, the detection must be above the  $2\sigma$  level in that band. Following Sawangwit & Shanks (2010a) we ensure that the sources are genuinely point sources by matching to the 5GHz ( $\approx 4'.6$  resolution) catalogues from the Greenbank Northern sky Survey (GB6, Gregory et al. 1996), or Parkes-MIT-NRAO (PMN, Griffith & Wright 1993), surveys. The *WMAP* team also provide a 7 yr CMB-free catalogue as described by Gold et al. (2011). This catalogue has been created with the objective of detecting point sources free of boosting by CMB fluctuations. We proceed with the raw 5-band catalogue with 471 sources and a CMB-free catalogue with 417 sources.

## 3 PLANCK RADIO SOURCE FLUXES AND SZ CLUSTER DECREMENTS

### 3.1 Conversion of Radio Flux to Temperature Profiles

The *Planck* ERCSC provides us with the source flux density, error and a few parameters on the source characteristics and detection. To enable us to translate the *Planck* fluxes into *WMAP* observables we need to convert the source flux density,  $S_{tot}$ , into an observed peak Rayleigh-Jeans antenna temperature using the conversion factor  $\Gamma^{ff}(\nu)$  (Page et al. 2003),

$$\Delta T_{RJ}(0) = S_{tot} \Gamma^{ff}(\nu), \quad (1)$$

where

$$\Gamma^{ff}(\nu) = \frac{c^2}{2k_b \nu_e^2} \frac{1}{\Omega_{beam}(\nu)}. \quad (2)$$

Here  $\nu_e$  is the effective frequency of the bandpass and the  $ff$  superscript denotes the fact that the majority of the *WMAP* sources have a spectral index  $\alpha \approx -0.1$ , approximately that of free-free emission.

The *WMAP* temperature maps are given in terms of

the thermodynamic temperature. At the *WMAP* frequencies and CMB temperature, the Rayleigh-Jeans temperature is appreciably different from this. We therefore correct between the two temperature differences, using eq(3), where  $x' = h\nu/k_b T_{cmb}$  and  $T_{cmb} = 2.725\text{K}$  is the monopole temperature of the CMB (Jarosik et al. 2003).

$$\begin{aligned} \Delta T_t &= \frac{(e^{x'} - 1)^2}{x'^2 e^{x'}} \Delta T_{RJ}, \\ &= g(\nu) \Delta T_{RJ}. \end{aligned} \quad (3)$$

The observed *WMAP* temperature profiles therefore take the form,

$$\begin{aligned} \Delta T(\theta) &= \Delta T(0) b^s(\theta), \\ &= g(\nu) \Gamma^{ff} S_{tot} b^s(\theta). \end{aligned} \quad (4)$$

We see the beam dependence of the observed profile is twofold. The shape is dependent on the symmetrized beam profile  $b^s(\theta)$  (normalised to unity at  $\theta = 0^\circ$ ), while the scale is normalised by the beam solid angle associated with  $\Gamma^{ff}$ . A summary of the assumed values of  $g(\nu)$  and  $\Gamma^{ff}$  is provided in Table 2.

### 3.2 *Planck* SZ Decrements

*Planck* presents its observed decrements using an SZ model fit parameterised by the total SZ signal within the cluster extent. Here we briefly describe this model so that the *Planck* results can be compared to the stacked *WMAP* temperature decrements.

Clusters are significant reservoirs of gas which will result in a SZ distortion to the CMB described by the Compton  $y$  parameter,

$$\Delta T(\theta) = T_{cmb} j(x') y(\theta). \quad (5)$$

Here,  $j(x')$  is the spectral function, where  $x' = h\nu/k_b T_{cmb}$  (Sunyaev & Zeldovich 1980),

$$j(x') = \frac{x'(e^{x'} + 1)}{e^{x'} - 1} - 4. \quad (6)$$

The integrated  $Y$  parameter is the total SZ signal, which is simply the integration of the Compton  $y$  parameter on the sky,

$$Y = \int y d\Omega. \quad (7)$$

Alternatively, if we integrate over the cluster volume,

$$Y = \frac{\sigma_t}{m_e c^2} \int P dV. \quad (8)$$

However, we are observing a 2-D projection of the cluster<sup>2</sup> on the sky. The angle  $\theta$  we observe on the sky, corresponds in 3-D to a cylindrical bore through the cluster of radius  $R = \theta D_a(z)$ , where  $D_a$  is the angular diameter distance.

<sup>2</sup> The cluster is assumed to be spherical.

The observed integrated  $Y$  parameter therefore takes the form (Arnaud et al. 2010),

$$\begin{aligned} Y_{cyl}(R) &= \frac{\sigma_t}{m_e c^2} \int_0^R 2\pi r dr \int_r^{R_{tot}} \frac{2P(r') r' dr'}{(r'^2 - r^2)^{1/2}}, \\ &= Y_{sph}(R_{tot}) - \frac{\sigma_t}{m_e c^2} \int_R^{R_{tot}} 4\pi P(r) (r^2 - R^2)^{1/2} r dr. \end{aligned} \quad (9)$$

To predict the SZ effect implied by eq(9) we have to make a choice of the pressure profile,  $P(r)$ . Historically it has been common to fit the SZ profile with an isothermal  $\beta$  model, (Cavaliere & Fusco-Femiano 1976). However, X-ray observations have shown that the assumption of an isothermal gas breaks down at the cluster outskirts, (Pratt et al. 2007; Piffaretti et al. 2005). To account for this additional complexity, Nagai, Vikhlinin, & Kravtsov (2007) therefore proposed using a Generalised NFW (GNFW) profile for the pressure instead. The profile is scale invariant in that it is independent of absolute distances and is instead a function of the dimensionless scale  $x = R/R_{500}$ . The profile takes the form,

$$\mathcal{P}(x) = \frac{P_0}{(c_{500} x)^\gamma [1 + (c_{500} x)^\alpha]^{(\beta - \gamma)/\alpha}}, \quad (10)$$

where  $\mathcal{P}(x) = P(r)/P_{500}$  and  $P_{500}$  is the characteristic pressure defined by Arnaud et al. (2010).

Here we have a five parameter fit to the pressure profile,  $[P_0, c_{500}, \gamma, \alpha, \beta]$ . This allows independent specification of the pressure in the cluster core ( $\gamma$ ), main-body ( $\alpha$ ) and outskirts ( $\beta$ ). In Table 3 we outline the parameters used by *Planck*, as taken from Arnaud et al. (2010). The characteristic parameters of the cluster are  $M_{500}$ ,  $P_{500}$ ,  $R_{500}$  (see Appendix A) where the 500 denotes the fact they are evaluated within the region where the mean mass density is 500 times greater than the critical density  $\rho_{crit}(z)$ . The *Planck* team extract the integrated  $Y$  parameter using the Multifrequency Matched Filter (MMF3) method (*Planck* Collaboration et al. 2011d) based on the above self-similar model. The integration is done to the angular cluster extent corresponding to  $5R_{500}$ , which *Planck* also report ( $\theta_{5R_{500}}$ ). Their errors on the integrated SZ signal,  $Y$ , combine their estimated measurement error with Monte-Carlo estimates of the error due to uncertainties within the self-similar model (Melin, Bartlett, & Delabrouille 2006).

### 3.3 SZ Temperature Profile Reconstruction

We now proceed to invert the *Planck* data to provide us with expected *WMAP* temperature profiles. (See Appendix A for the details of this derivation). From the *Planck* values for  $Y(5R_{500})$  and  $\theta_{5R_{500}}$ , and using  $J(x)$  and  $I(x)$ , the cylindrical and spherical SZ templates (see eq.(A7)) we first obtain  $Y_{cyl}(R)$  via eq.(A9),

$$Y_{cyl}(R) = Y_{cyl}(5R_{500}) \left( 1 - \frac{J(x)}{I(5)} \right). \quad (11)$$

From this integrated  $Y_{cyl}(R = \theta \cdot D_A(z))$ , we want to derive the angular dependence of the Compton  $y$  parameter, where  $y(\theta) = \frac{d}{d\Omega} Y_{cyl}(\theta)$ , and so

Type	$P_0$	$c_{500}$	$\gamma$	$\alpha$	$\beta$
All:Fitted	$8.403(\frac{h}{0.7})^{-\frac{3}{2}}$	1.177	0.3081	1.0510	5.4905

**Table 3.** Summary of the *Planck* NFW parameters as used in eq. (10) and described by Arnaud et al. (2010). These are the same parameters as used by the *Planck* team, the All:Fitted set.

$$y(\theta) = -\frac{Y_{cyl}(5R_{500})}{I(5)} \frac{d}{d\Omega}(J(x)). \quad (12)$$

The self-similar model therefore predicts an SZ temperature decrement,

$$\Delta T_{SZ}(\theta) = -T_{cmb} j(x') \frac{Y_{cyl}(5R_{500})}{I(5)} \frac{d}{d\Omega}(J(x)), \quad (13)$$

where  $Y_{cyl}(5R_{500})$  is the integrated  $Y$  given in the ESZ.

### 3.4 Convolution with the WMAP beam profile

The cluster profile is not directly observed by *WMAP* and is instead smoothed by the instrument response. The predicted *WMAP* SZ profile therefore results from the 2-D convolution of eq.(13) with the *WMAP* beam profile. Myers et al. (2004) and Bielby & Shanks (2007) assumed that the source is well resolved with respect to the *WMAP* beam. Under this assumption the full form for a 2-D convolution can be approximated by a 1-D convolution<sup>3</sup>. However, the typical cluster sizes used in SZ studies are of the same order as the *WMAP* beams and so this approximation can start to fail. Furthermore, for profiles such as the self-similar model which are very centrally peaked this approximation becomes increasingly invalid. The implementation of the PSF convolution used in this paper is fully 2-D and does not rely on such approximations. In Section 9.4 we explore the impact of this on the Bielby & Shanks (2007) results.

## 4 CROSS-CORRELATION METHODS

### 4.1 Stacking Positions

The choice of coordinates to use for the radio source positions and cluster centres is important. Scatter or an offset in the centroid used in the cross-correlation could cause the stacked result to appear artificially broad or induce artifacts. However, the only sample used in this paper for which astrometric errors are appreciable are the *WMAP* derived radio-source catalogues where the astrometric error in both longitude and latitude is  $4'$  (Chen & Wright 2009). We mitigate for this effect by using the position of the corresponding matched 5GHz source, since these have negligible astrometric error  $\mathcal{O}(10'')$  (Gregory et al. 1996; Griffith & Wright 1993).

<sup>3</sup> Taking a Gaussian beam as an example, if  $\sigma_{beam}$  is much smaller than the typical scale of the cluster profile then the  $\theta$  integral in Bailey & Sparks (1983)'s eq.(2) which describes the non-radial aspect (ie: the 2-D nature) of the convolution is approximately  $2\pi$ . This effectively reduces the dimensionality of the convolution, which now takes a 1-D Gaussian form.

We find no evidence for an offset between the *WMAP* and 5GHz sources and hence we are confident that astrometry error will not cause new broadening of the beam. We also note that the stacking procedure we use is dominated by the brighter objects, which typically have better astrometry.

For the *Planck* radio source catalogues we have used the *Planck* positions since these are of high astrometric quality (*Planck* Collaboration et al. 2011exp). In our sample selection we have rejected sources which the *Planck* team estimate to have relatively high astrometric errors. The effect of this selection in the 100GHz band is to ensure that  $\sigma < 0'.75$  for the  $S \geq 1.1$ Jy sample.

For the *Planck* ESZ objects we have taken the *Planck* estimated positions rather than the X-ray derived positions as the cluster centres. We do this to avoid the complications associated with rare but potentially large offsets between the SZ and X-ray signals which are likely caused by merging events (*Planck* Collaboration et al. 2011d).

### 4.2 Calculation of Profiles

Our cross-correlation/stacking procedures for measuring both radio point source profiles and SZ decrements are similar to those of Myers et al. (2004), Bielby & Shanks (2007) and then as updated by Sawangwit & Shanks (2010a). Ultimately, we shall be stacking/cross-correlating *WMAP* data around radio source positions and cluster centres from catalogues, particularly from the *Planck* ERCSC. To estimate a temperature profile for an individual source  $j$  we use,

$$\Delta T_j(\theta) = \sum_i \frac{T_{ij}(\theta) - \bar{T}_j}{n_{ij}(\theta)}, \quad (14)$$

where the sum is over the pixels, denoted  $i$ , within a circular annulus of radius  $\theta$ . Here  $n_{ij}$  represents the number of pixels within the annulus and  $T_{ij}$  is the temperature recorded for the pixel  $i$  and source  $j$ .  $\bar{T}_j$  is the average background temperature which can either be estimated locally in a surrounding annulus in a ‘photometric method’ or globally (see Sawangwit & Shanks 2010a). These two background estimates make no difference in the stacked results but can make a difference for individual sources (see Section 9). We then stack the *WMAP*7 data by averaging  $\Delta T_j(\theta)$  over the sources that have pixels within the annulus  $\theta$  using the statistical average,  $\Delta T(\theta) = \sum_j (1/N_\theta) \Delta T_j(\theta)$ .  $N_\theta$  is the number of sources that have pixels within the annulus  $\theta$  and is usually constant for all except the  $\theta \lesssim 4'$  bins.

We have followed Sawangwit & Shanks (2010a) in using jack-knife errors, for both the radio and SZ sources, based on 6 equal area sub-fields defined by lines of constant galactic longitude and split by the galactic equator. For  $N = 6$  fields denoted  $k$ , the errors are,

$$\sigma^2(\theta) = \frac{N-1}{N} \sum_k \left( \Delta T_k(\theta) - \overline{\Delta T}(\theta) \right)^2, \quad (15)$$

where  $\Delta T_k(\theta)$  is the average of the fields excluding field  $k$ . We have experimented with both alternative sub-fields and methods such as bootstrap resampling finding approximately equivalent results. In Section 7.1 we have used simulations to test whether our method can robustly recover the

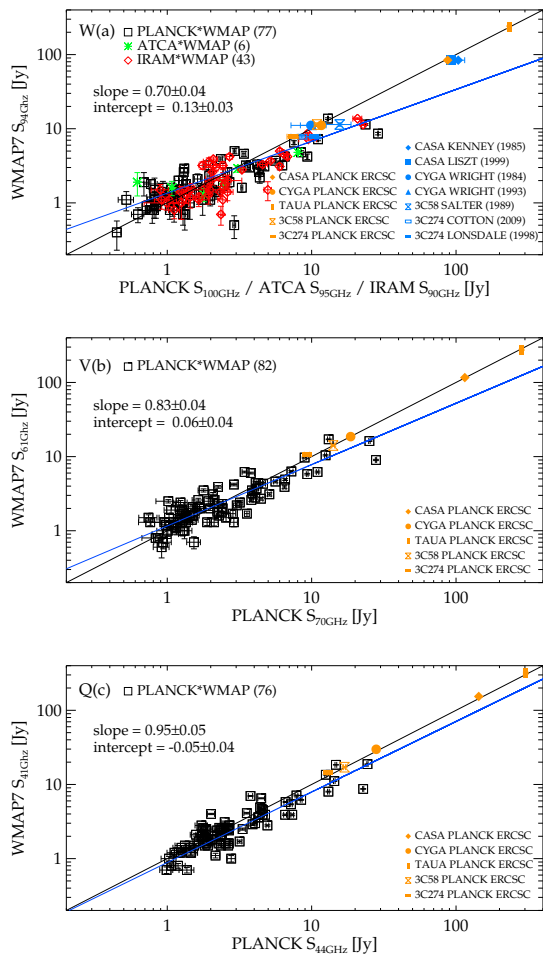


**Figure 1.** A comparison between the *WMAP7* fluxes, *Planck* and ground based source fluxes. Also shown are the one-to-one relation (black line) and the best fit relation (blue line). Measurements of the Weiland et al. (2011) sources have been corrected to a *WMAP* epoch of 2005 and the respective *WMAP* band-centres using the Weiland et al. (2011) variability estimates and spectral indices.

beam profile, in doing so we find that our jack-knife errors are reasonable.

## 5 FLUX COMPARISONS

### 5.1 Gold et al. (2011) *WMAP7* and *PLANCK* ERCSC

We first compare *WMAP7* sources at Q, V, W from Gold et al. (2011) to their counterparts in the *Planck* ERCSC at 100, 70 and 44 GHz. We also compare the *Planck* fluxes in the 100GHz band to the ground-based ATCA and IRAM source fluxes previously used by Sawangwit & Shanks (2010a).

In Fig. 1 we first focus on the comparison of the *WMAP7* fluxes to *Planck* and also the ground-based ATCA and IRAM sources. We only consider the matches with separation less than  $2'$  to avoid any possible systematic errors associated with sources that have poor astrometry. However,

our results are independent of this cut up to separations of  $10'$ . At high fluxes we see evidence for a systematically lower *WMAP* flux,  $\approx 50\%$  above 2Jy. This non-linearity is particularly prominent in the W band, the band with the greatest angular resolution.

Since there are errors in both variables we have used the Numerical Recipes (Press et al. 1992) *fitexy* as our fitting routine. We find best fit logarithmic slopes of  $[0.70 \pm 0.04, 0.83 \pm 0.04, 0.95 \pm 0.05]$  for the [100GHz-W, 70GHz-V, 44GHz-Q] comparisons. To obtain realistic errors on these fits we have linearly scaled the flux errors until we obtained a  $\chi^2$  probability of 0.5 as recommended by Press et al. (1992), for data with a dominant intrinsic dispersion.

Clearly, *Planck* and *WMAP* fluxes for sources were measured at different times. Since at least  $\approx 30\%$  of the *WMAP5* radio sources exhibit some level of variability (Wright et al. 2009), we expect and observe much larger scatter than accounted for by the estimated flux uncertainty. However, we note that the brighter *WMAP* sources are fainter than the one-to-one relation, this is in the opposite sense expected if variability was biasing faint *Planck* sources into the *WMAP* catalogue when in a bright phase.

We investigate whether variability is alternatively causing a bias due to *Planck* dropouts by limiting the *WMAP* sample to  $\geq 5\sigma$  sources. The advantage is that the *Planck* team have investigated all the *WMAP*  $\geq 5\sigma$  objects that are not in the ERCSC. They conclude that for the 100GHz-W comparison the missing objects are ‘all’ spurious and can be explained by the object having a weak or missing 5GHz ID (*Planck* Collaboration et al. 2011exp). The resulting  $\geq 5\sigma$  *WMAP* W-band sample of 48 sources (with  $S \geq 0.8Jy$ ) is therefore complete in the sense of being 100% represented in the *Planck* sample with no bias due to a *Planck* dropout population. When we then repeat the *WMAP-Planck* 100GHz-W flux comparison, we find a logarithmic slope of  $(0.67 \pm 0.05)$ , consistent with the original result and therefore strong evidence against a highly variable source population causing dropouts that bias the *WMAP-Planck* comparison.

The disagreement between *Planck* and *WMAP* is in contrast to direct comparisons between *Planck* and ground-based ATCA/IRAM data. These instead show good agreement, as shown in Fig. 2 for the *Planck* 100GHz radio point sources. The best fit logarithmic slope of  $[0.95 \pm 0.05]$  is statistically consistent with the one-to-one relation. However, comparing *WMAP* W-band and the ground-based ATCA/IRAM data we find evidence for non-linearity with a best fit logarithmic slope of  $[0.72 \pm 0.04]$ . These contrasting fits are particularly significant because the greatest *Planck-WMAP* non-linearity comes from the 100GHz-W flux comparison. Given the agreement between *Planck* and the ground-based ATCA/IRAM observations, we interpret the flux disagreement as being due to *WMAP*.

### 5.2 Further tests for bias

In response to the referee we have made additional bootstrap and jack-knife re-sampling tests of the *WMAP\*Planck* flux-flux comparison and its error. After 1000 bootstrap resamplings we estimate logarithmic slopes of  $[0.70 \pm 0.09, 0.84 \pm 0.11, 0.96 \pm 0.10]$  for the [100GHz-W, 70GHz-V, 44GHz-Q] comparisons. We also perform Jackknife resamplings of the

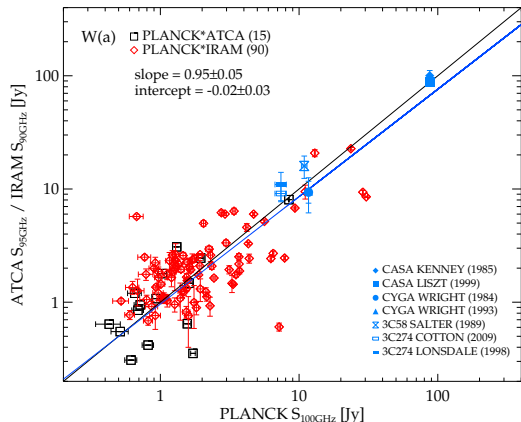


**Figure 2.** A comparison of the 100GHz *Planck* fluxes and the ground-based sources. Also show are the one-to-one relation (black line) and the best fit relation (blue line). Measurements of the Weiland et al. (2011) sources have been corrected to a *Planck* ERCSC epoch of 2010 and the respective *Planck* band-centres using the Weiland et al. (2011) variability estimates and spectral indices.

*WMAP*\**Planck* flux-flux comparison, we estimate a logarithmic slope of  $[0.70 \pm 0.10, 0.83 \pm 0.12, 0.95 \pm 0.10]$  for the  $[100\text{GHz-W}, 70\text{GHz-V}, 44\text{GHz-Q}]$  comparisons. These resampling results are consistent with our original samples and support the accuracy of our previous error analysis.

We have also made Monte-Carlo simulations of the flux-flux comparison. We generated samples with the same number of sources as in the real flux-flux comparison using the *WMAP* Q-band power-law distribution,  $N(< S) \propto S^{-1.7}$ , (Bennett et al. 2003). These fluxes are then scaled to the respective *WMAP* and *Planck* band centres on the basis of a Gaussian distribution in spectral indices,  $\alpha$ , with mean  $-0.09$  and standard deviation  $0.176$ , (Wright et al. 2009). Realistic Gaussian measurement errors are then assigned as a function of flux in a manner consistent with the original *WMAP* and *Planck* samples. To include variability we start from the Wright et al. (2009) analysis of the *WMAP5* data that measured a median rms flux variability for the 25 brightest Q-band objects of  $\sigma = 0.23$  and which we therefore additionally apply to all our sources, assuming a Gaussian distribution. We then impose detection limits corresponding to the faintest source in the given band for the *WMAP* and *Planck* fluxes respectively. Finally, we compare these two flux types by measuring the best fit relation in the same way as was originally done for the *Planck*-*WMAP* comparison. After 10,000 simulations of the 100GHz-W comparison we find average logarithmic slopes and intercepts of  $[0.98 \pm 0.06]$  and  $[0.04 \pm 0.06]$ . These results are not only in agreement with a one-to-one relation but support the errors found in our original *WMAP*-*Planck* comparison. We therefore conclude we are able to robustly recover the expected one-to-one result and hence that our comparison may be unbiased.

### 5.3 Potential contamination of *Planck* fluxes by CO emission

*Planck* Collaboration et al. (2011exp) have noted that the

100GHz bandpass contains the  $J = 1 \rightarrow 0$  rotational CO emission line. This is a potential explanation for the flux non-linearity we report between the *WMAP* 94GHz W-band and *Planck* 100GHz bands. However, such an explanation would imply that *WMAP* and *Planck* are in agreement away from the galactic plane where CO emission is lower. However, we see no evidence for such a distinction, with galactic latitude cuts of  $|b| > 5^\circ$ ,  $|b| > 30^\circ$  and  $|b| > 45^\circ$  we find 100GHz-W logarithmic slopes of  $[0.70 \pm 0.04]$ ,  $[0.65 \pm 0.06]$ , and  $[0.72 \pm 0.08]$  respectively.

### 5.4 Inclusion of the 5 additional Weiland et al. (2011) bright sources

Weiland et al. (2011) have made a comparison of *WMAP* fluxes of bright radio source fluxes from ground-based telescopes and claim that they support the *WMAP* flux scale. Some of the sources used are planets and have not been through the same reduction procedures as the CMB maps but five other sources, Cyg A, Cas A, Tau A, 3C58 and 3C274 have gone through the same procedures. Weiland et al. (2011) selected these sources on the basis that they were the brightest and least variable of the sources with adequate background contrast and a history of prior observation.

We now expand our flux comparisons by including<sup>4</sup> these Weiland et al. (2011) sources in Fig. 1. We use the *WMAP* fluxes quoted by these authors and the independent ground-based fluxes that are mostly those quoted by these authors. We see that in the W band at least, *WMAP* also underestimates the flux of these sources (blue points) and indeed Cyg A, 3C274 and 3C58 appear not inconsistent with our fitted relation. However, the underestimation for Cas A is less than predicted by extrapolating the fit to the brighter radio fluxes. If this result were to be more highly weighted then there would still be evidence for a *WMAP* flux problem, but one which now looked more like a constant offset than a scale error. However, we note that there are differences between the two ground-based observations of Cas A. Furthermore, Cas A lies close to the galactic plane ( $|b| < 6^\circ$ ) and hence contamination might be an issue. It may therefore be too early to infer a flux offset on the basis of this source.

When we include the Celestial sources from Weiland et al. (2011) with independent ground-based measurements<sup>5</sup> into the *Planck*-*WMAP* comparison we find logarithmic slopes of  $[0.86 \pm 0.08, 0.90 \pm 0.10, 0.98 \pm 0.09]$  for the  $[100\text{GHz-W}, 70\text{GHz-V}, 44\text{GHz-Q}]$  comparisons. After Jack-knife and bootstrap resampling we find logarithmic slopes of  $[0.81 \pm 0.10, 0.83 \pm 0.12, 0.95 \pm 0.10]$  and  $[0.81 \pm 0.08, 0.84 \pm 0.11, 0.986 \pm 0.10]$  respectively for the  $[100\text{GHz-W}, 70\text{GHz-V}, 44\text{GHz-Q}]$  comparisons. Hence, whilst including the Celestial source data changes the degree of the non-linearity, the results are still in significant disagreement with a one-to-one relation.

We finally add the *Planck* ERCSC measurements of

<sup>4</sup> We do not include Tau A because it lacks a *WMAP* independent measurement to compare to at the W,V,Q frequencies.

<sup>5</sup> We do not include measurements without error estimates, this excludes the Cyg A Wright & Sault (1993) and 3C274 Lonsdale et al. (1998) measurements



these 5 sources to Fig. 1 and Fig. 2. This complicates the picture further since they appear to agree with the *WMAP* results more than the ground-based results. As far as we can see, the *Planck* fluxes are not calibrated via *WMAP*. If we then fit the full *Planck-WMAP* W band comparison we now find less evidence for a discrepancy between the two finding a 100GHz-W logarithmic slope of  $[0.91 \pm 0.04]$ . But just making the 100GHz-W comparison in the 3-400Jy region, the result might then again look more like a constant offset with a logarithmic slope and intercept of  $[1.01 \pm 0.10]$  and  $[0.16 \pm 0.12]$ .

We conclude that the *WMAP* fluxes in the  $S \approx 10$ Jy region show systematically lower fluxes than *Planck* and we have argued that this discrepancy is unlikely to be explained by variability, underestimated errors or inaccurate flux estimation. At lower and higher fluxes the *WMAP-Planck* agreement seems better, implying some non-linearity in their relative scales. If *WMAP* data are compared to ground-based data rather than *Planck*, the same discrepancy is seen at  $S \approx 10$ Jy and a small but significant discrepancy is seen at brighter fluxes, which would more imply a linear offset rather than a non-linearity. Similar effects are seen at Q and V but at a lower level.

## 6 WMAP POINT SOURCE PROFILES

### 6.1 *Planck* ERCSC radio sources

We now apply the stacking analysis of Sawangwit & Shanks (2010a) to the co-added *WMAP7* maps, centring on the *Planck* radio point sources. *Planck* sources are selected at multiple wavebands which may be advantageous in avoiding spurious sources etc. Figs. 3 (a),(b),(c) are shown for completeness because these raw temperature plots demonstrate the main uncertainty in this analysis which is the accuracy of the background subtraction. We note that there is some difference between the global background and the background local to the source samples but generally this effect appears smaller in the *WMAP7* data (eg at W) than it was in the *WMAP5* datasets used by Sawangwit & Shanks (2010a).

Figs. 3 (d),(e),(f) show the same profiles now background subtracted and scaled to unity at the origin to produce  $b^S(\theta)$ . We have used the ‘photometric’ subtraction to produce the radio point source temperature profile,  $\Delta T_{radio}(\theta)$ . For the *WMAP7* dataset there is very little difference in the profiles resulting from global or local/photometric background subtractions.

These  $b^S(\theta)$  are now compared to the *WMAP* Jupiter beam and the best fit beam to the bright *WMAP* radio source profiles found by Sawangwit & Shanks (2010a) (dashed orange line in their Fig. 2). There is again evidence that the *Planck* selected radio sources suggest a wider beam than the Jupiter beam, particularly in the W band, although the *Planck* sources lie slightly below the profile fits from Sawangwit & Shanks (2010a). We further note that the statistical significance of the deviations from the Jupiter beam for the *Planck* selected sources at  $12'.6 - 19'.9$  is only modest at  $\approx 2 - 3\sigma$  for the W band.

The normalisation of  $b^S(\theta)$  to unity at small scales forms a further uncertainty in these beam comparisons. In Figs. 3 (g),(h),(i) we have applied the formalism of Section 3.1 and

attempted to make absolute normalisations of the various model profiles, using the *Planck* ERCSC listed fluxes. We assume in turn the Jupiter profile and then the radio source profile of Sawangwit & Shanks (2010a) in calculating the resulting  $\Gamma^{ff}$  factor. These give respectively the blue and red lines. Hence, if the radio sources followed the Jupiter profile, for example, we should see the same peak temperature for the stacked model profile and the stacked data. We see that the *Planck* peak temperatures, particularly in the W band, tend to lie between the Jupiter profile and the previous *WMAP* bright radio source fits. These results suggest that the previous radio source fit may be too wide at  $\theta > 30'$  where it is essentially an extrapolation, unconstrained by the data, and this will affect the accuracy of its absolute normalisation i.e. there is a large error in  $\Omega_{beam}$ . Otherwise, the conclusion is similar to that from Figs. 3 (d),(e),(f) in that the *Planck* data is suggesting that the Jupiter beam is a poor fit to the radio source profiles particularly at W.

The question of Eddington bias was discussed by Sawangwit & Shanks (2010a) and has also been suggested by Schultz & Huffenberger (2011) as a possible explanation of the wide radio profiles. In terms of the *Planck* sources an Eddington bias of  $\approx 0.02$ mK is required to explain our results. However our pre-selection of these sources as being point-like at *Planck* resolution and our rejection of both faint ( $S < 1.1$ Jy) and CMB-contaminated sources mean that it is difficult to see how Eddington bias could be affecting these results. In Fig. 3 (d),(e),(f) we have also presented the source sample without the  $S \geq 1.1$ Jy flux cut. The consistency of the full source and brighter source samples indicates that Eddington bias is not significantly affecting these samples.

### 6.2 *WMAP7* radio sources

We next repeat the analysis of Sawangwit & Shanks (2010a) using the co-added *WMAP7* maps and source catalogue (Gold et al. 2011). The results are shown in Fig. 4. We see that the results again tend to lie between the Jupiter profile and the previous *WMAP* bright radio source fits by Sawangwit & Shanks (2010a). This may in part be due to the *WMAP7* profiles returning to zero at large scales more uniformly than *WMAP5*, making the differences between the photometric and global profile estimates more marginal. However, we also found that using the *WMAP5/WMAP7* catalogue in the *WMAP7/WMAP5* temperature maps gives profiles more consistent with the Sawangwit & Shanks (2010a) fits. We therefore attribute the difference between Fig. 4 and the results of Sawangwit & Shanks (2010a) to a possible systematic difference between *WMAP5* and *WMAP7*, with perhaps a contribution from statistical fluctuations.

Following Sawangwit & Shanks (2010a) we minimised any effect of Eddington bias for this sample by pre-selecting only sources that appear in the 5GHz GB6 and PMN radio samples. We have only used 5GHz coordinates for the radio sources, with their sub-30'' accuracy to minimise any positional error in our analysis. Although Eddington bias may well be affecting the faintest *WMAP* sources, as was also noted in Sawangwit & Shanks (2010a), we have used a flux limit of  $S \geq 1.1$ Jy. In Section 7.1 we shall check for the



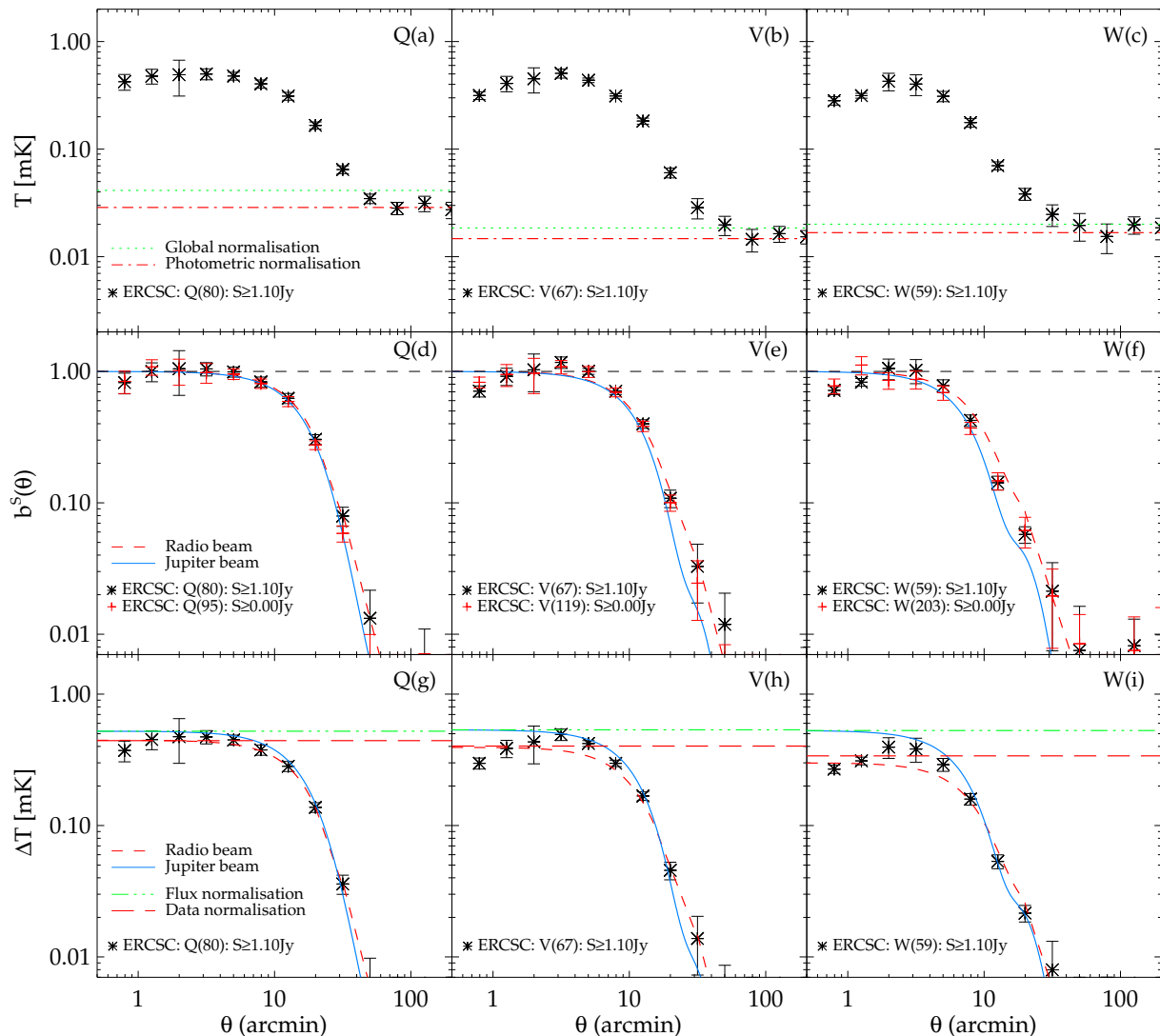


**Figure 3.** (a),(b),(c): The raw stacked *WMAP7* [Q,V,W] temperature profiles for the *Planck* [44,70,100] GHz band sources with the global mean and photometric background temperatures of the map plotted as dashed (green, red) lines. (d),(e),(f): The photometrically subtracted, stacked and re-normalised *WMAP7* [Q,V,W]  $b^s(\theta)$  profiles for the *Planck* [44,70,100] GHz band sources. Also shown are the  $b^s(\theta)$  for the Jupiter beam (blue, solid) and the radio source fit (red, dashed) of Sawangwit & Shanks (2010a). Any sensitivity to Eddington bias is shown in the profiles without the flux limit of  $S \geq 1.1\text{Jy}$  (lighter red, cross). (g),(h),(i): The photometrically subtracted and stacked *WMAP7* [Q,V,W]  $\Delta T(\theta)$  profiles for the *Planck* sources. Also shown are the  $\Delta T(\theta)$  for the Jupiter beam (blue, solid) and the radio source fit (red, dashed) of Sawangwit & Shanks (2010a), now absolutely normalised via the *Planck* flux.

presence of Eddington bias in this particular dataset using random simulations.

### 6.3 WMAP7-CMBfree radio sources

In the ‘CMB-free’ method (Chen & Wright 2009), *WMAP* sources are selected using the Q,V,W bands simultaneously to form an internal linear combination map (ILC) with weights chosen to cancel out the CMB anisotropy signal. Again, any Eddington bias due to CMB fluctuations should be reduced in the case of this point source catalogue. We therefore repeated our stacking analysis with the 417 QVW sources from the Gold et al. 2011 *WMAP7* ‘CMB-free’ catalogue (see Fig. 5). Overall we again see wider-than-expected

profiles at W, broadly consistent with the results in Figs. 3, 4. Finally, we have also presented these results without the  $S \geq 1.1\text{Jy}$  flux limit, we note that the result is unchanged. This consistency is evidence for robustness of the result to Eddington bias.

### 6.4 NVSS radio sources

Point source catalogues made at significantly lower frequencies than the *WMAP* bands are unlikely to be affected by Eddington bias due to CMB fluctuations, if identification is done independently of the *WMAP7* point source catalogue. For example, point sources selected at 1.4 GHz will have Rayleigh-Jeans temperature  $\approx 4500\times$  higher than a

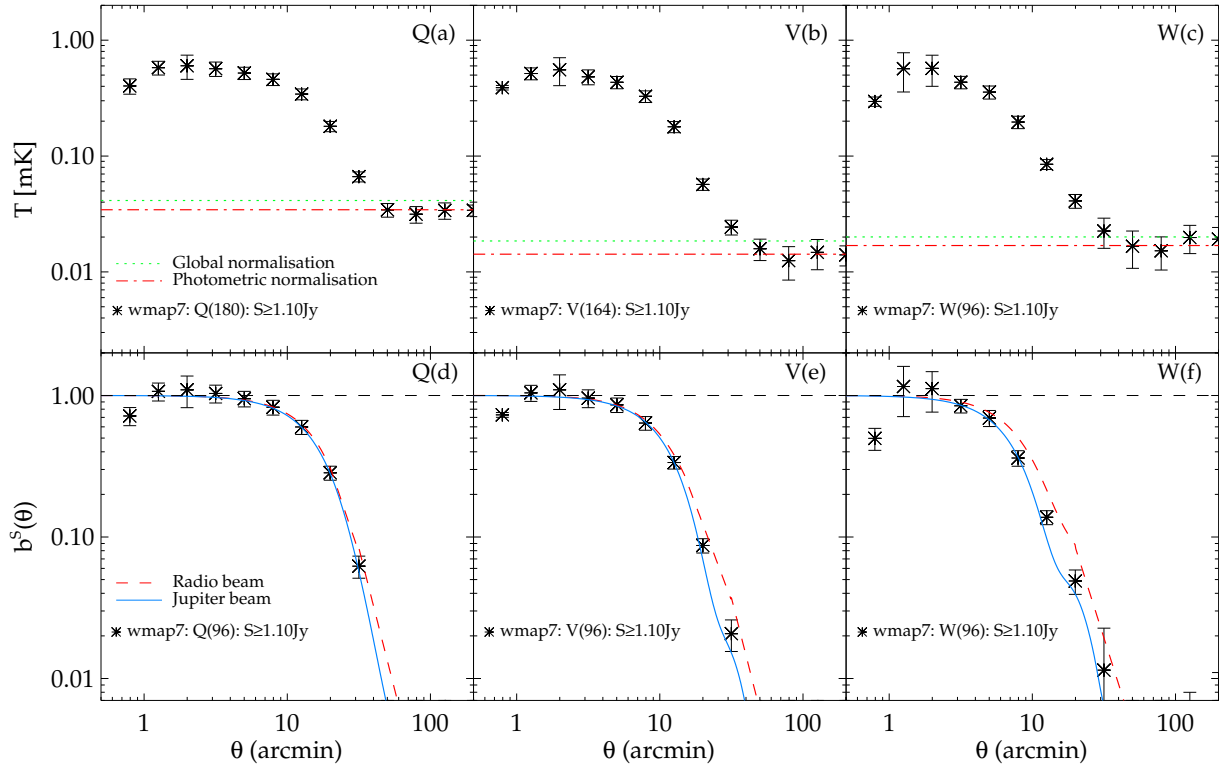


**Figure 4.** (a),(b),(c): The raw stacked *WMAP7* [Q,V,W] temperature profiles for the *WMAP7* sources of Gold et al. (2011) with the global mean and photometric background temperatures of the map plotted as dashed (green, red) lines. (d),(e),(f): The photometrically subtracted, stacked and re-normalised *WMAP7* [Q,V,W]  $b^s(\theta)$  profiles for the *WMAP7* sources of Gold et al. (2011). Also shown are the  $b^s(\theta)$  for the Jupiter beam (blue, solid) and the radio source fit (red, dashed) of Sawangwit & Shanks (2010a).

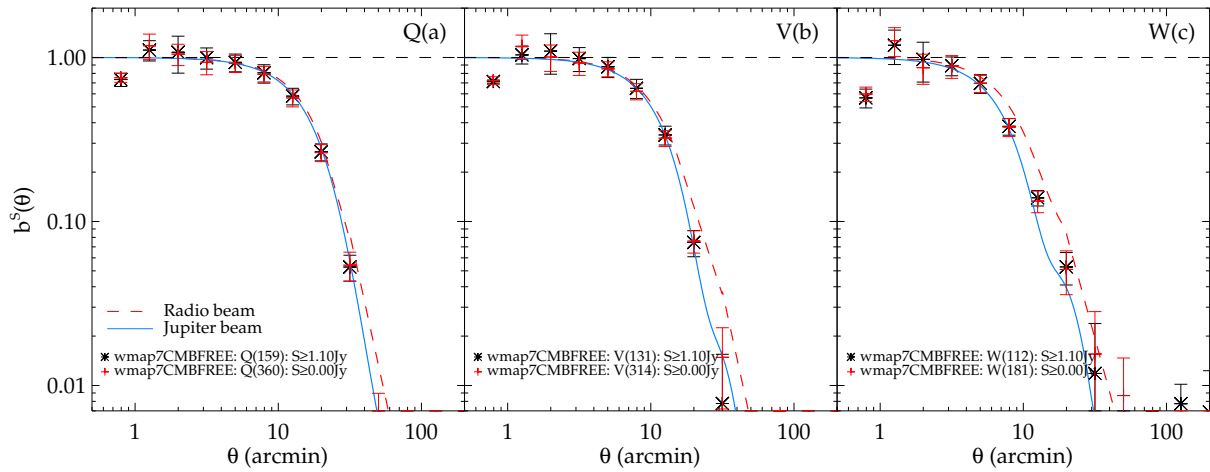


**Figure 5.** (a),(b),(c): The photometrically subtracted, stacked and re-normalised *WMAP7* [Q,V,W]  $b^s(\theta)$  profiles for the CMB-free *WMAP7* catalogues of Gold et al. (2011). Also shown are the  $b^s(\theta)$  for the Jupiter beam (blue, solid) and the radio source fit (red, dashed) of Sawangwit & Shanks (2010a). Any sensitivity to Eddington bias is shown in the profiles without the flux limit of  $S \geq 1.1\text{Jy}$  (lighter red, cross).

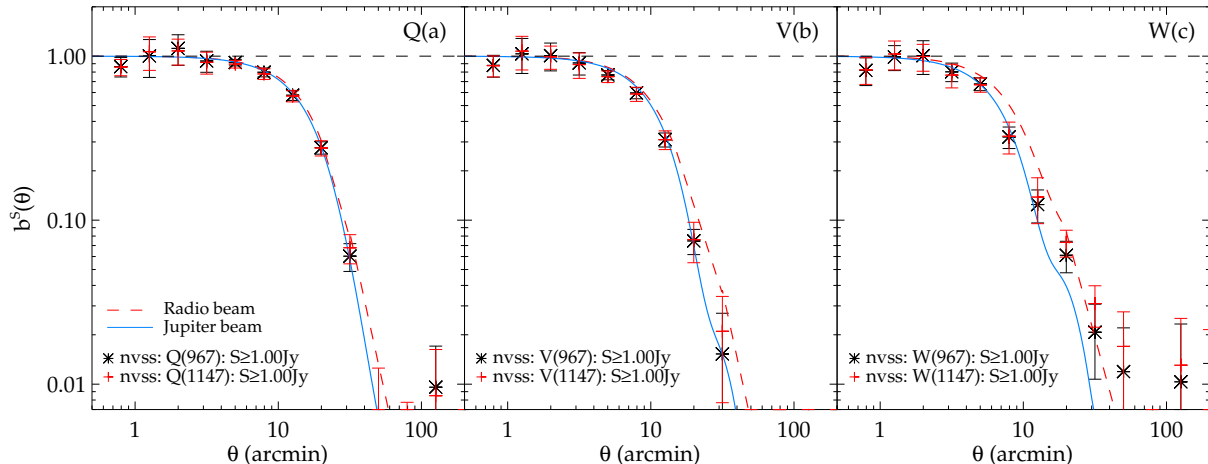


**Figure 6.** (a),(b),(c): The photometrically subtracted stacked *WMAP7* [Q,V,W]  $b^s(\theta)$  profiles for the NVSS sources. Also shown are the  $b^s(\theta)$  for the Jupiter beam (blue, solid) and the radio source fit (red, dashed) of Sawangwit & Shanks (2010a).

source with similar flux density selected at W-band ( $\approx 94$  GHz), i.e.  $T_{RJ} \propto \Omega_{beam}^{-1} \nu^{-2}$ , whereas the rms Rayleigh-Jeans temperature due to the CMB fluctuations stays roughly the same between the two frequency bands, (Bennett et al. 2003). Therefore, we now stack co-added *WMAP7* temperature data centred around the positions of the 1147  $S_{1.4} > 1$  Jy NVSS point sources. Fig. 6 shows the resulting Q, V and W profiles. We see that they are consistent with those measured using *WMAP5* total/bright sources in Fig. 2 of Sawangwit & Shanks (2010a). However, the profiles do not appear as wide as the *WMAP5* faintest subsample despite the average flux of the NVSS sample at *WMAP* bands being  $\approx 3\times$  lower.

Many of the NVSS sources are resolved into multiple components (Blake & Wall 2002). However, this is unlikely to cause the widening of the beam beyond  $\theta \gtrsim 6'$ . Here, as a precautionary measure, we shall test the beam profile measured using the NVSS by excluding any source that has neighbouring source(s) within  $1^\circ$ . This extra condition reduces the number of  $S_{1.4} > 1.0$  Jy sources outside the *WMAP7* ‘point source catalogue’ mask to 967. The resulting co-added beam profiles are also shown in Fig. 6. We see that the beam profiles are in good agreement with the previous results.

## 7 WMAP AND NVSS SOURCE CATALOGUE SIMULATIONS

### 7.1 Description

We made 100 Monte Carlo simulations to check our method and the robustness of the results. These simulations are due to Sawangwit (2011) who made them in the context of his test of the W1 beam in the *WMAP5* dataset. Thus they are conservative in terms of both the errors they imply and the test of Eddington bias they make in our new context of the averaged DA’s (W1-W4 in the W-band case) and the *WMAP7* dataset. We followed the procedures described by Wright et al. (2009) (see also Chen & Wright 2009). For

each set of simulations,  $\approx 10^6$  point sources are generated with a power-law distribution,  $N(> S) \propto S^{-1.7}$ , at *WMAP* Q-band (Bennett et al. 2003; Chen & Wright 2009). Their spectral indices,  $\alpha$ , are drawn from a Gaussian distribution with a mean -0.09 and standard deviation 0.176 as characterised by the *WMAP5* point source catalogue (Wright et al. 2009). The flux density for each object is scaled to the centre of the other four bands using the relation  $S_\nu \propto \nu^\alpha$ . The source positions are then randomly distributed on the sky and each source is assigned to a pixel in a HEALPix  $N_{side} = 2048$  map. For a source with flux density  $S_\nu$ , the peak Rayleigh-Jeans temperature difference,  $\Delta T_{RJ}(0)$ , is given by eqs.(1, 2), but with the  $\Omega_{beam}$  replaced by  $\Omega_{pix} = 2.5 \times 10^{-7}$  sr, solid angle of a  $N_{side} = 2048$  pixel. The publicly available *WMAP* maps (Section 2.2) are given in thermodynamic temperature (Limon et al. 2008). For a direct comparison with our results, we thus convert the simulated source’s  $\Delta T_{RJ}(0)$  to  $\Delta T_i(0)$  using eq.(3).

Five temperature maps, one for each band, are then smoothed with the corresponding *WMAP* beam transfer function (Hill et al. 2009) before being downgraded to  $N_{side} = 512$ . The simulated CMB temperature map (smoothed with an appropriate beam transfer function) constructed from *WMAP5* best-fit  $C_\ell$  and pixel noise are then added to the source temperature maps. The pixel noise is modelled as a Gaussian distribution with zero mean and standard deviation  $\sigma = \sigma_0/\sqrt{N_{obs}}$ , where  $N_{obs}$  is the number of observations in each pixel and  $\sigma_0$  is given for each DA and frequency band (Limon et al. 2008). Here, we use the *WMAP5*  $N_{obs}$  map to generate pixel noise for its corresponding band map.

### 7.2 Source Detection

Next, we applied the five-band detection technique following procedures utilised by *WMAP* team (Bennett et al. 2003; Gold et al. 2011). Firstly, the temperature maps are weighted by the number of observations in each pixel,  $N_{obs}^{1/2}$ . The weighted map is then filtered in harmonic space

by  $b_\ell / (b_\ell^2 C_\ell^{\text{CMB}} + C_\ell^{\text{noise}})$  (e.g. Tegmark & de Oliveira-Costa 1998; Refregier, Spergel, & Herbig 2000) where  $C_\ell^{\text{CMB}}$  is the CMB power spectrum and  $C_\ell^{\text{noise}}$  is the noise power, and  $b_\ell$  is the beam transfer function (Hill et al. 2009). The filter is designed to suppress fluctuations due to the CMB at large scales and pixel noise at scales smaller than the beam width. We used the *WMAP5* best-fit  $C_\ell$  for  $C_\ell^{\text{CMB}}$ . The  $C_\ell^{\text{noise}}$  are determined from pixel noise maps constructed using  $\sigma_0$  and five-year  $N_{\text{obs}}$  for each band as described above. We then search the filtered maps for peaks which are  $> 5\sigma$ . Peaks detected in any band are fitted to a Gaussian profile plus a planar baseline in the unfiltered maps for all other bands. The recovered source positions are set to the best-fit Gaussian centres in W-band. The best-fit Gaussian amplitude is converted to Rayleigh-Jeans temperature, using the relation given in eq.(3), and then to a flux density using conversion factors,  $\Gamma^{ff}(\nu)$ , given in Table 4 of Hill et al. (2009). In any given band, we only use sources that are  $> 2\sigma$  and the fitted source width smaller than 2x the beamwidth, following the *WMAP* team. The number of detected sources from 100 realisations are consistent with *WMAP5* point source analyses by Wright et al. (2009) and Chen & Wright (2009). Our simulations also recover the input power-law  $N(> S)$  distribution down to the expected *WMAP5* limit,  $S \approx 1$  Jy, remarkably well (see Sawangwit 2011).

### 7.3 *WMAP* simulation results

For each simulation we applied our beam profile analysis outlined in Section 4 (including a flux cut of  $S > 1.1\text{Jy}$ ). The average beam profiles derived from 100 simulations are plotted in Fig. 7(a)-(c) where the error bar represents their standard deviation in each angular bin. We found that even profiles as narrow as the W1-band Jupiter profile can be retrieved remarkably well out to  $30'$ . The estimated uncertainties using these Monte Carlo simulations are consistent with the jack-knife error estimations. Note that the Monte Carlo error converges after  $\approx 60$ -70 simulations. The Monte Carlo simulations we performed here suggests that our method for recovering beam profile by stacking temperature maps around point sources is robust and the jack-knife error estimation is reliable.

### 7.4 NVSS simulation results

Although we argued above that sources (i.e. their identifications and positions) selected at NVSS frequency are robust against the CMB fluctuations compared to *WMAP* bands, our beam analysis is still carried out using *WMAP* temperature maps. As we noted, the average flux of the  $S_{1.4} > 1\text{Jy}$  NVSS sources in the *WMAP* bands is  $\approx 3\text{x}$  lower than the *WMAP* sample. Therefore it is important to check whether the *WMAP* beam profiles can be robustly recovered using these NVSS sources. Again the results come from Sawangwit (2011) and were only applied to the W1 detector assembly and use *WMAP5* data.

We again created 100 Monte Carlo simulations similar to those described above but without the five-band detection procedure since these sources are pre-detected by NVSS with high positional accuracy ( $\lesssim 1''$ , Condon et al. 1998). The 967 NVSS source positions are used and fluxes at 1.4

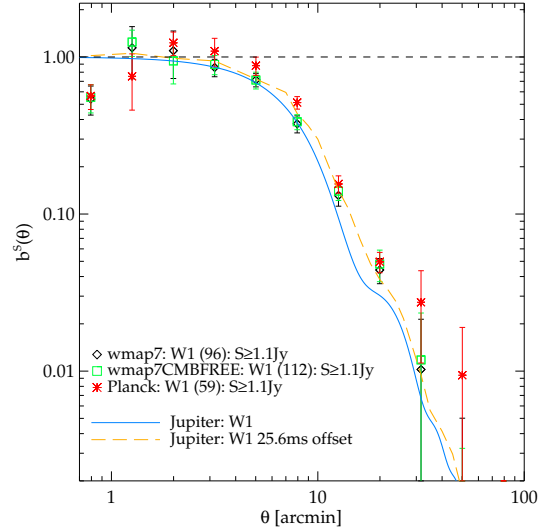


**Figure 8.** The photometrically subtracted, stacked and re-normalised *WMAP7* [Q1,V1,W1]  $b^s(\theta)$  profiles for the *Planck*, *WMAP7* and CMB-free *WMAP7* catalogues. Also shown are the  $b^s(\theta)$  for the Jupiter beam (blue, solid) and a model showing the effect of a 25.6ms timing offset on the W1 Jupiter beam (orange, dashed) Sawangwit (2011).

GHz are extrapolated to *WMAP* Q, V and W bands assuming a mean spectral index,  $\alpha$ , of -0.45 in order to mimic the average flux density observed in these bands. The temperature maps are smoothed with the corresponding *WMAP* (Jupiter) beam profiles. The simulated CMB fluctuations and radiometer noise are then added to the source temperature maps as described above. For each *WMAP* band, we applied our beam profile analysis to each of the 100 simulated maps (including a flux cut of  $S_{1.4} > 1\text{Jy}$ ). The results are shown in Fig. 7(d)-(f). The plot shows that with these NVSS radio sources the *WMAP* beam profiles can be robustly recovered out to  $30'$  and are not affected by the source clustering consistent with the semi-empirical calculation presented in Sawangwit & Shanks (2010a). We then take the standard deviation of the 100 simulated results in each angular bin as the  $1\sigma$  error. The ratio of the Monte Carlo error to the jack-knife error is shown as the dotted line in Fig. 7(d)-(f). The Monte Carlo and jack-knife errors are in good agreement except at scales  $< 10'$  where jack-knife errors are somewhat over-estimates in Q and V bands.

The simulations suggest that when flux limited at  $S \geq 1.1\text{Jy}$ , the *WMAP* selected source profiles are unaffected by Eddington bias. The simulations also support the accuracy of our empirical errors. The simulations suggest the same conclusions apply when dealing with flux-limited ( $S_{1.4} > 1\text{Jy}$ ) NVSS data.

## 8 POSSIBLE EXPLANATIONS OF WIDE RADIO SOURCE PROFILES

We now briefly consider possible explanations for the radio source profiles we have observed. We start by accepting that in the *WMAP7* data the profiles are less wide than found in the *WMAP5* data discussed by Sawangwit & Shanks

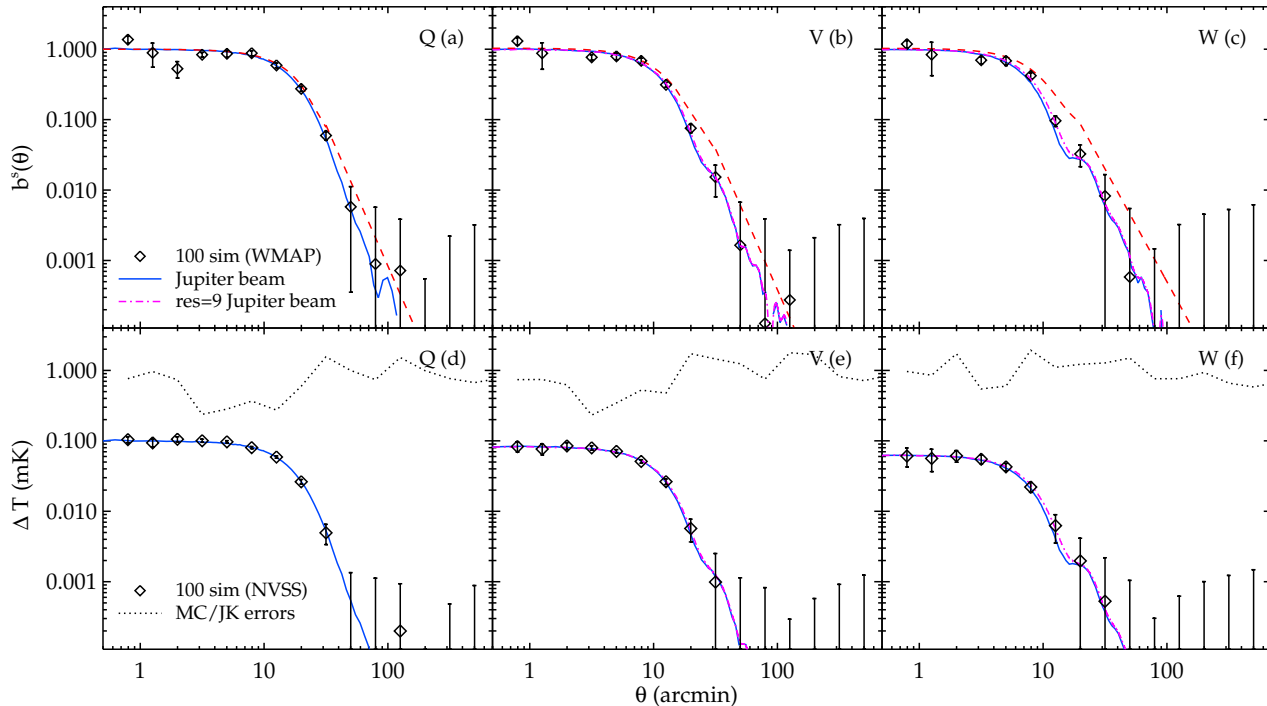


**Figure 7.** (a),(b),(c): The recovered [Q1,V1,W1] beam profiles using simulated *WMAP* point sources. The error bars are  $1\sigma$  rms of 100 simulations. The effect of pixelisation on the profile measurement is shown by the magenta dot-dashed lines. (d),(e),(f): Similar to (a-c) but now using  $S_{1.4} > 1$  Jy NVSS sources and without the re-normalisation. The ratios between Monte Carlo and jack-knife errors are shown as the dotted lines.

(2010a). We regard our best current result to come from comparison with the *Planck* radio sources where we have checked the sources against spatial extension at *Planck* resolution and also rejected any that are contaminated by the CMB. This sample still rejects the W-band Jupiter beam at  $\approx 2 - 3\sigma$  significance at  $12'.6 - 19'.9$ , about the same as the rejection of the previous best fit model from Sawangwit & Shanks (2010a). Therefore it is not outside the bounds of possibility that the previous result may be explained by a statistical fluctuation in the *WMAP5* data. However, at the suggestion of the referee, we have now evaluated the rejection significance of the Jupiter beam using the full covariance matrix from our simulations, fitting in the range  $4' < \theta < 20'$ . For the Jupiter beam in the 7yr coadded maps we find formal rejection significances from the  $\chi^2$  distribution of  $[1.5^{-3}, 4.5^{-4}, 1.2^{-3}, 1.4^{-6}]$  for *Planck*, *WMAP7*, *WMAP7*-CMBfree and NVSS respectively. Although we note that the overlap between these samples means that these results cannot be simply combined, individually these probabilities correspond to  $\gtrsim 3\sigma$  rejections of the Jupiter beam.

It is therefore still worth considering whether a wider beam could be related to other possible *WMAP* data problems. The first of these is the possible disagreement in *WMAP* flux comparisons with ground-based and *Planck* datasets noted by Sawangwit & Shanks (2010a) and also in this paper. Certainly a non-linearity like we first fitted to Fig. 1 goes in the right direction to explain a flatter than expected profile. Indeed, if the addition of Cas A, Cyg A, Tau A, 3C274 and 3C58 does imply that *WMAP* fluxes are

simply offset from *Planck* and ground-based fluxes, then flux comparisons would be consistent with the wide beam. A logarithmic intercept of  $\approx -0.1$  implies the *WMAP* flux is  $\approx 80\%$  of the corresponding *Planck* flux. Equally, we find the W-band *WMAP* Jupiter beam solid angle is  $\approx 80\%$  of the 25.6 ms timing offset derived beam's  $\Omega_{beam}$ . This is in agreement with the expectation from eq.(1) that at fixed temperatures (ie: those provided in the *WMAP* maps)  $S_{tot} \propto \Omega_{beam}$ .

However, more data at brighter fluxes is needed to check if the *WMAP* flux is non-linear or simply offset with respect to other datasets. We note that Malik et al. (in prep) has used the CMB dipole to look for non-linearity in the *WMAP* temperature scale and failed to find any evidence for such an effect.

The second possible explanation for the wider than expected radio source profiles focused on the possibility that there was a timing offset between the *WMAP* antenna pointing and temperature data, as proposed by Liu & Li (2011). As well as causing effects at large scale due to a wrongly subtracted dipole, this scan pattern offset would cause a wider beam profile (see Moss, Scott, & Sigurdson 2011). Sawangwit (2011) have calculated the beam pattern that a 25.6 ms timing offset would cause in the W band. The calculation assumes the W1 Jupiter beam and takes into account its initial asymmetry on the sky. After creating simulated *WMAP* TOD that include point sources distributed in ecliptic latitude and then applying mapmaking to these data, Sawangwit (2011) found the azimuth averaged beam profiles shown in Fig. 8 for both zero timing offset and the 25.6ms timing offset with the latter giving a

reasonable fit to the *Planck* data. More details are presented by Sawangwit (2011). These include further results based on using the dependence of beam shape with ecliptic latitude to try and determine the timing offset which marginally prefer zero timing offset. We note that Roukema (2010) made similar tests based on bright *WMAP* sources and found no evidence for a timing offset at the map-making stage. On the other hand, Liu & Li (2011) checked between offsets by minimising dipole residuals and found strong evidence for a non-zero offset, see Sawangwit et al (in prep). We note that the *WMAP* team have indicated that they use a timing offset of zero in which case the above agreement would simply represent a coincidence.

## 9 SZ RESULTS

### 9.1 *Planck* Intermediate Results

Our final aim is to make a comparison between the *Planck* ESZ and *WMAP* SZ results as described in Section 3.2, 3.3 and 3.4. However this involves reverse engineering the *Planck* SZ  $\Delta T(\theta)$  profiles. We therefore first use recently released *Planck* SZ data to check our reverse engineered *Planck* profiles. A series of papers have been released as a follow up to the *Planck* ESZ data. Two papers in particular are relevant to corroborating the *Planck* profiles presented in this paper. In *Planck* Collaboration et al (2012X) the *Planck* Coma SZ profile has been published. Additionally, the ‘physical’ *Planck* SZ temperature profiles for the 62 local clusters (LSZ) in the *Planck* Collaboration et al. (2011g) analysis have been published in *Planck* Collaboration et al. (2012V). Below, we compare our reverse engineered profiles to these *Planck* data.

#### 9.1.1 *Planck* Collaboration et al (2012X)

In Fig. 9 we now compare our *Planck* Coma SZ profiles to *Planck* Collaboration et al (2012X). We have shown two alternative *Planck* models in order to display the sensitivity of our results to the cluster size estimates. This is motivated by the significant difference between the value of  $R_{500} = 1.31\text{Mpc}$  used in *Planck* Collaboration et al (2012X) and the ESZ value,  $R_{500} = 1.13\text{Mpc}$ . Since the value for the integrated SZ signal,  $Y(5R_{500})$ , is degenerate with cluster size the ESZ value for  $Y(5R_{500})$  cannot be assumed. Therefore, in the first instance we do show an expected *Planck* temperature decrement using the ESZ values and calculated using eq.(13). However, we also show a model which uses an alternative method for calculating the expected *Planck* profile. Here, the *Planck* Collaboration et al (2012X) value of  $R_{500}$  is used to calculate  $Y_{500}$  which can then be used to set the profile amplitude as shown in eq.(A8). This method is solely dependent on the cluster size estimate, and is further described in Appendix A.

We find agreement between the Coma self-similar SZ model and the observed *Planck* temperature profiles. Although the *Planck* data does seem to have both a lower central amplitude and a slightly wider profile at large angular scales than the self-similar expectation. We note that corresponding differences between the self-similar model and the *Planck* data can be seen in the *Planck* Collaboration et al

(2012X) analysis. A flatter inner profile may also be expected if any pixelisation effects cause any further smoothing beyond the stated resolution of  $10'$ . We also find reasonable agreement between our two estimates of the *Planck* profile that use different cluster size estimates. Although, as expected, the model using the *Planck* Collaboration et al (2012X) value of  $R_{500}$  does provide a better fit to the *Planck* data. We conclude that the agreement between our *Planck* expectation and the underlying *Planck* profile supports the validity of our inversion of the *Planck* ESZ data to obtain *Planck* temperature profiles.

#### 9.1.2 *Planck* Collaboration et al. (2012V)

In Fig. 10 we compare our *Planck* ‘physical’ SZ profiles for the 62 *Planck* Collaboration et al. (2011g) clusters to the ‘physical’ *Planck* profiles presented in *Planck* Collaboration et al. (2012V). As was previously shown in *Planck* Collaboration et al. (2012V) the *Planck* [100,70,44] GHz profiles are in agreement with the self-similar expectation. We now expand on this by attempting to use these results to verify our method of inverting the *Planck* ERCSC data to obtain *Planck* temperature profiles.

Since we again find that the *Planck* Collaboration et al. (2011g) estimates of cluster size can be significantly different from the ESZ estimates we have used an alternative method of obtaining expected *Planck* temperature profiles. This method replicates *Planck* Collaboration et al. (2012V)’s approach in assuming the Arnaud et al. (2010) self-similar model for the cluster and directly evaluating the Compton-y parameter, as outlined in Appendix A. We have further followed *Planck* Collaboration et al. (2012V)’s Section. 4.3 in using the *Planck* Collaboration et al. (2011g) estimates of  $\theta_{500}$  and calibrate the central GNFW pressure,  $P_0$ , using the X-ray equivalent of the integrated SZ signal,  $Y_X$ .

As shown in Fig. 10 the two self-similar models convolved with  $10'$  FWHM Gaussian beam profiles are in agreement beyond  $R_{500}$ . However the inner profile of *Planck* Collaboration et al. (2012V)’s model (black, solid  $\pm$  dotted) is substantially sharper than our model (green, solid). Although our model lies within the *Planck* Collaboration et al. (2012V)’s  $\approx 1\sigma$  dispersion, we are comparing the stacked models (ie: the statistical average) so the error range is a  $\sqrt{N} \approx 8$  smaller. We believe this difference is caused by the different stacking procedure used in *Planck* Collaboration et al. (2012V) where depending on the noise properties within the bin either logarithmic or linear weightings were used. We have found that using these alternative weightings can accentuate the central peak of the profile, although not to the extent necessary for full agreement with *Planck* Collaboration et al. (2012V). We currently do not have a full explanation for the difference in central amplitude.

## 9.2 *WMAP-Planck* ESZ comparison

We next show the stacked *WMAP*7 temperature profiles for 151 clusters listed in the *Planck* ESZ catalogue. We are using the ‘photometric’ approach to background subtraction, with an annulus from  $60' - 120'$  being used in W (and scaled according to beamwidth in Q and V). The final models are based on the statistical average of the clusters.



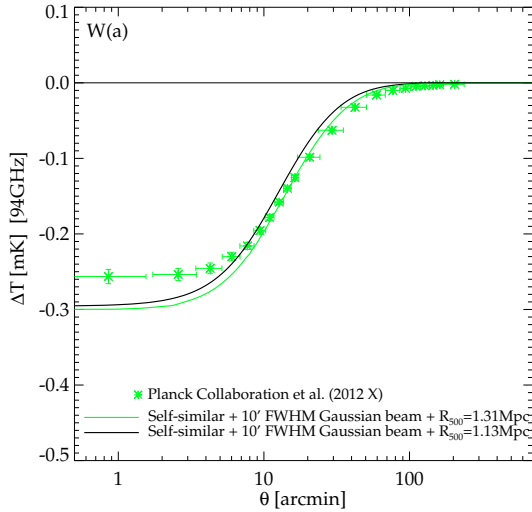


**Figure 9.** (a): The *Planck* Collaboration et al (2012X) *Planck* SZ decrement for the Coma cluster converted from RJ temperatures to a thermodynamic temperature at 94GHz. Also shown are the *Planck* temperature decrements from eq.(13) using the ESZ value of  $R_{500}$  (black, solid) and eq.(A8) using the *Planck* Collaboration et al (2012X) value of  $R_{500}$  (green, solid). Both models are convolved with a 10' FWHM Gaussian beam appropriate to the *Planck* Collaboration et al (2012X) data.

We see in Fig. 11 that the *WMAP* data is an excellent fit to the *Planck* expectation. The fit between the *Planck* data and the *WMAP* data is not only good in all three [W,V,Q] bands but at all angular scales. We have further quantified the SZ measurements using jack-knife and bootstrap techniques all of which support *WMAP-Planck* agreement, however we acknowledge these techniques don't include covariance.

In Fig. 11 we have shown the *Planck* self-similar models convolved with the power-law beams from Sawangwit & Shanks (2010a). We find that in the case of the W band where the radio source profiles are most different from the Jupiter beam, there is now disagreement with the *WMAP* data with a deficit of  $\approx 20\%$  in the centre. In the Q and V bands where the radio source profiles are closer to the Jupiter beam, the wider beams give virtually no change in the agreement with the *WMAP* data. We conclude that the *Planck* SZ profiles disagree with the Sawangwit & Shanks (2010a) *WMAP*5 radio source profile fits.

However, the Sawangwit (2011) timing offset derived beam, which provides an excellent fit to the radio source profiles as shown in Fig. 8, is significantly less wide than the Sawangwit & Shanks (2010a) beam. As shown in Fig. 11 we find that the the timing offset beam only marginally reduces the central SZ temperature. We therefore conclude that the *WMAP* SZ results are not at sufficient S/N to differentiate between the timing offset derived and the Jupiter beams.

### 9.3 Coma

We have also looked at the *Planck* model fits for the Coma cluster and compared them to *WMAP*. Part of the moti-

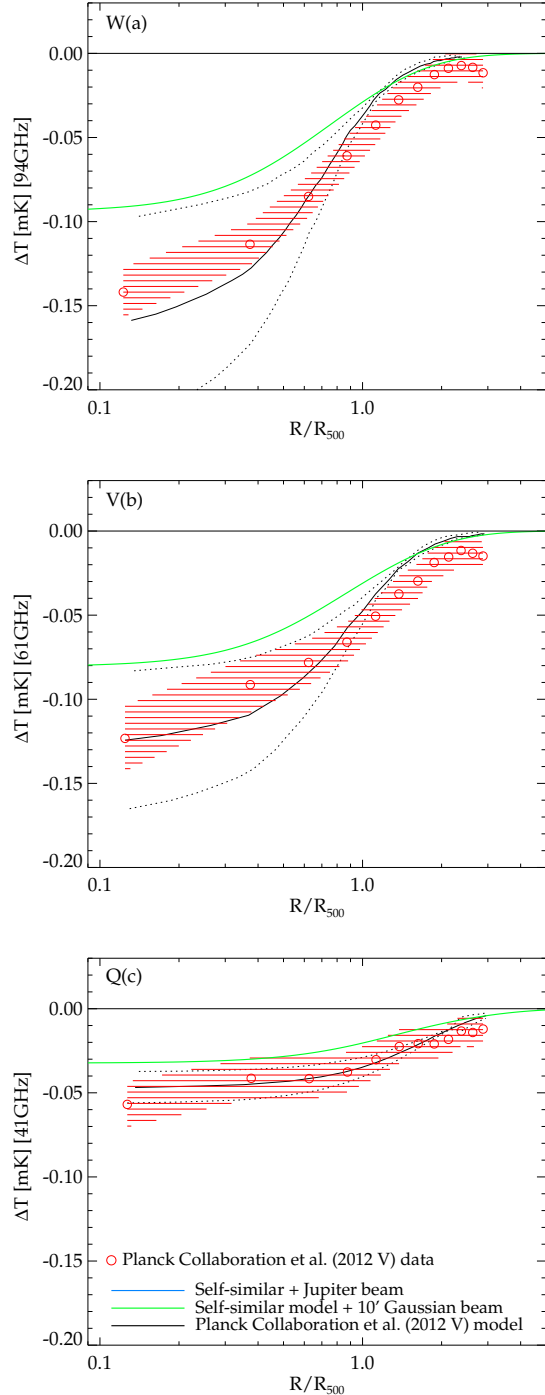


**Figure 10.** (a),(b),(c): The *WMAP* [W,V,Q] 'physical' SZ decrements for the 62 *Planck* Collaboration et al. (2011g) clusters compared to the *Planck* temperature decrement from eq.(13). The *Planck* profile is shown convolved with a 10' FWHM Gaussian (green, solid). We also show the 100GHz *Planck* profiles presented in *Planck* Collaboration et al. (2012V) converted into thermodynamic temperature at the *WMAP* band centre (red, stripes). The *Planck* Collaboration et al. (2012V) models (black, solid) are plotted with their associated dispersions (black, dotted).



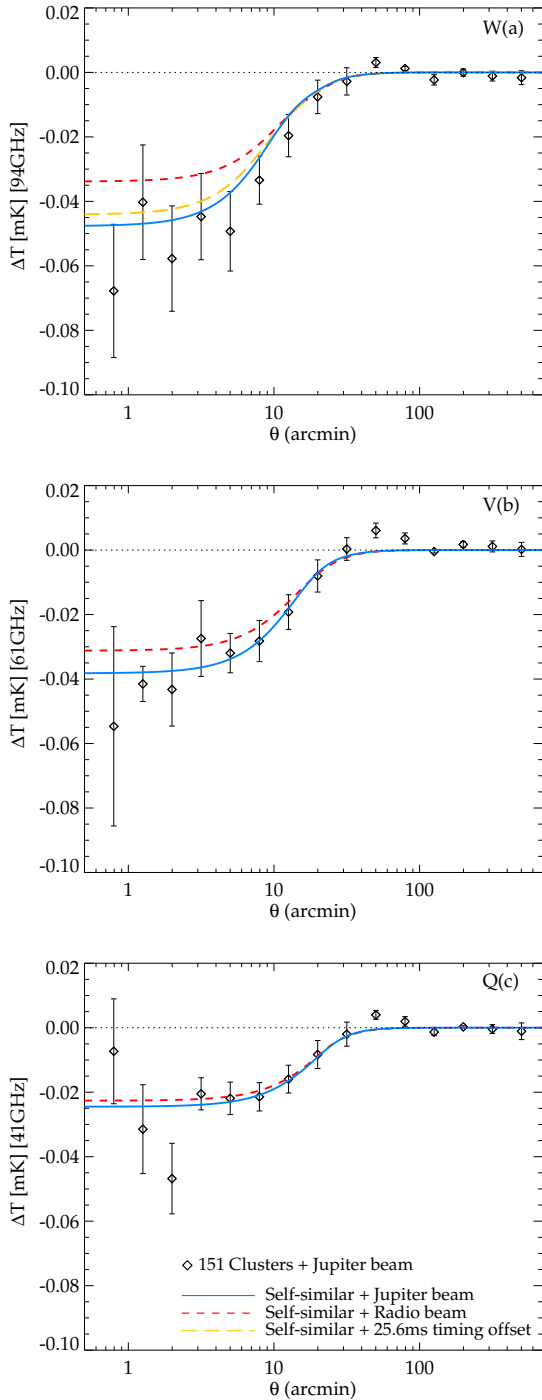


**Figure 11.** (a),(b),(c): The stacked *WMAP* [W,V,Q] SZ decrements for 151 *Planck* SZ clusters compared to the stacked *Planck* temperature decrement from eq.(13). The *Planck* profile is shown convolved with a *WMAP* Jupiter beam, a beam fitted to the radio source profiles by Sawangwit & Shanks (2010a) and the Sawangwit (2011) timing offset derived beam.

vation here is that previous authors, Lieu, Mittaz, & Zhang (2006) and Bielby & Shanks (2007), have used Coma in investigating the consistency of the *WMAP* SZ signal with X-ray predictions.

In Fig. 12 we now show the *Planck* self-similar model for Coma (solid blue line) and see that it is substantially overestimated by the *WMAP* data. An analogous situation was found by Komatsu et al. (2011) in that the *WMAP* Coma V and W band profiles (potentially affected by CMB contamination) showed  $\mathcal{O}(100\mu K)$  more SZ signal than the optimal combined V and W profiles (free of CMB contamination).

Komatsu et al. (2011) proposed that Coma may sit on  $\mathcal{O}(100\mu K)$  downwards CMB fluctuation. Our results are entirely consistent with this interpretation because the *Planck* MMF method is essentially ‘CMB-free’ whereas our *WMAP* Coma data may still be contaminated by CMB fluctuations. On this basis we also show in Fig. (12) a simple alteration to the *Planck* Coma SZ self-similar model by including a Gaussian with amplitude  $-100\mu K$  and  $(\mu, \sigma) = (0', 60')$  to mimic the effect of a downwards CMB contribution centred on Coma (blue, dashed). Agreement with the *WMAP* data is improved when a CMB contamination term is included. We therefore conclude that the difference between the *Planck* and *WMAP* Coma SZ profiles is the result of CMB contamination.

#### 9.4 Bonamente et al. (2006) Results

In Bielby & Shanks (2007) a *WMAP* discrepancy with the SZ/X-ray results of Bonamente et al. (2006) was presented. This is of particular interest as the Komatsu et al. (2011) *WMAP* SZ discrepancy was largely associated with the inner profile. The Bonamente et al. (2006) results complement this because they are weighted heavily to small scales because of the high resolution of their interferometric observations. In Fig. 13 we have therefore presented a stack of the 36 Bonamente et al. (2006) clusters that are unmasked in the *WMAP* temperature maps. We now find good agreement between the *WMAP* SZ decrements and the Bonamente et al. (2006) SZ/X-ray expectation. This is in contradiction to the results of Bielby & Shanks (2007). We have found this is attributable to Bielby & Shanks (2007)’s assumption that the cluster is well resolved with respect to the *WMAP* beam. As discussed in Section 3.4 this assumption introduces a systematic error into their 1-D convolution with the *WMAP* beam profiles. We therefore now report no evidence for a *WMAP* SZ discrepancy with respect to the Bonamente et al. (2006) X-ray models.

## 10 DISCUSSION

The main criticism that was made of the previous results of Sawangwit & Shanks (2010a) was that the wide *WMAP* radio source profiles may be caused by Eddington bias (Eddington 1913). Essentially, low S/N sources detected in the *WMAP* data may be contaminated by upwards CMB fluctuations and not balanced by downwards fluctuations. This could explain the wider than expected profiles, particularly at faint fluxes.

There may be some evidence for Eddington bias in the

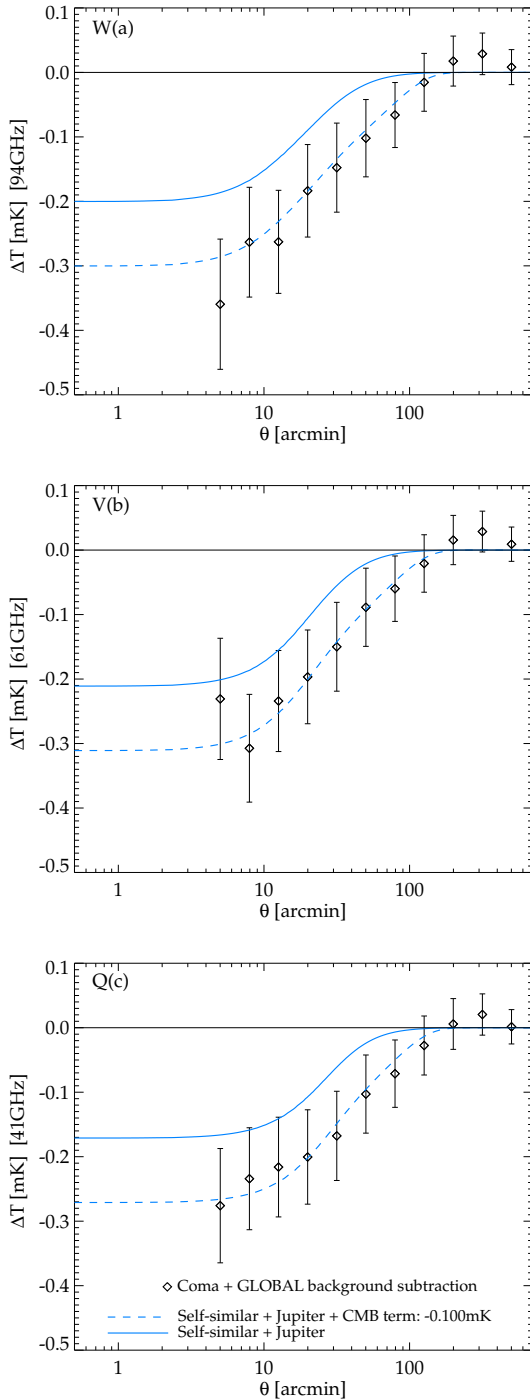


**Figure 12.** (a),(b),(c): The *WMAP* [W,V,Q] SZ decrements for the Coma cluster compared to the *Planck* temperature decrement from eq.(13). The error within each annulus for this individual cluster is simply the standard deviation of the ESZ clusters and is therefore only indicative. The *Planck* profile is shown convolved with a *WMAP* Jupiter beam (blue, solid). We also show a model incorporating a  $100\mu K$  downwards CMB fluctuation (blue, dashed).

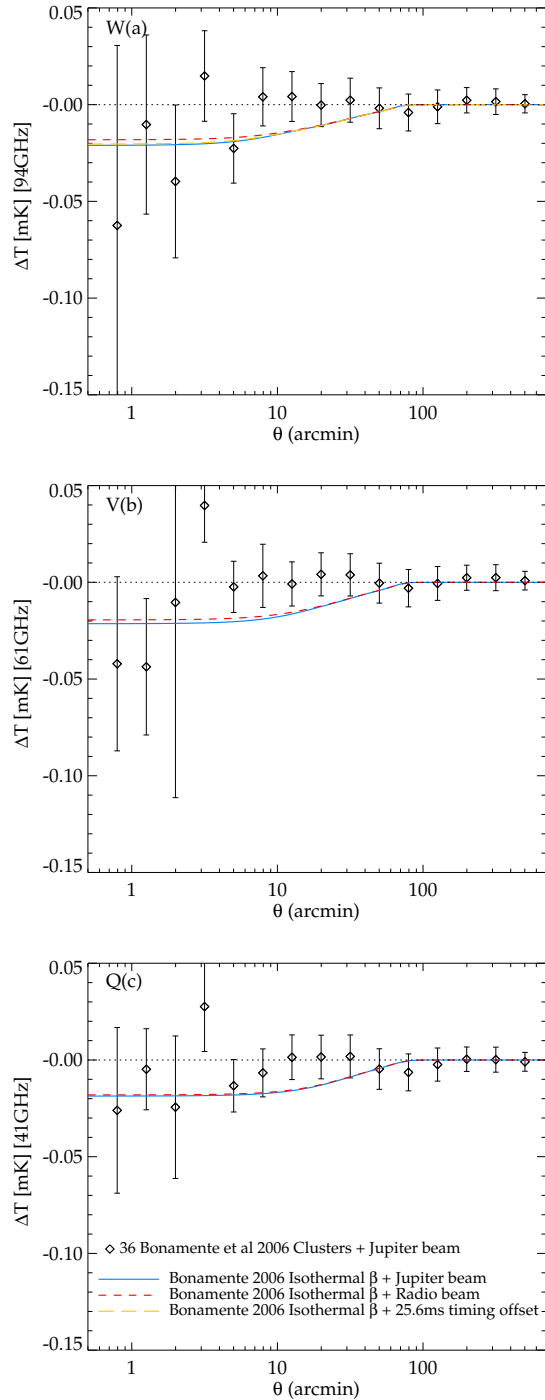


**Figure 13.** (a),(b),(c): The stacked *WMAP* [W,V,Q] SZ decrements for the 36 Bonamente et al. (2006) clusters that are unmasked in the *WMAP* temperature maps. This is compared to a stacked isothermal model based on the SZ/X-ray parameters fitted by Bonamente et al. (2006), convolved with the Jupiter beam, a beam fitted to the radio source profiles by Sawangwit & Shanks (2010a) and the Sawangwit (2011) timing offset derived beam.

faintest *WMAP5* W band source sub-sample that was initially used by Sawangwit & Shanks (2010a). However, it was because of this the faintest sources were not used in Sawangwit & Shanks (2010a) fits of the beam profile and that a flux limit of  $S \geq 1.1\text{Jy}$  has been used in calculating our radio source profiles. We also note that the *Planck* sources show the wider beam independent of whether the CMBSUBTRACT flag applies. We further note that we have restricted the *Planck* sources to have a FWHM strictly less than the *WMAP* W band beam profile width and find a wider than expected beam profile for these clearly point sources. *WMAP* sources selected from a ‘CMB-free’ map and NVSS selected sources at low frequency also show the same wider than expected beam.

Furthermore, we have also run Monte Carlo re-simulations of the source detection, producing artificial source catalogues extracted from simulated CMB maps. Here, after applying the same cross-correlation technique as for the data, the *WMAP* beam was recovered as input (see Fig. 7), again arguing that these sources are little affected by Eddington bias.

The *Planck* data also confirms the non-linearity of *WMAP* fluxes, particularly in the W band, in the range previously used. Decreasingly non-linear effects are also seen at Q and V. But when ground-based and *Planck* data for the bright Weiland et al. (2011) sources are included in these comparisons the evidence for non-linearity becomes less and it could still be that the discrepancy corresponds more to a constant offset.

Given that the beam profile widening is smaller in the *WMAP7* data than in *WMAP5*, a scan pattern timing offset as discussed by Liu & Li (2011) becomes a more plausible explanation for this effect. We have seen that the effect, originally invoked as an explanation for the alignment of the low order multipoles with the ecliptic, also provides a reasonable fit to the W band beam profiles (see Fig. 8).

In our comparison of *Planck*-*WMAP* SZ decrements we have found good agreement. Similarly, our *WMAP* SZ profile results are now in agreement with the X-ray data for the Bonamente et al. (2006) sample. This work is now in line with previous authors who when studying the integrated *WMAP* SZ signal  $Y_{tot}$  (as opposed to the Compton  $y$ -parameter) have found no evidence for a *WMAP* discrepancy (Melin et al. 2011). We have no explanation for the Komatsu et al. (2011) *WMAP* SZ profile discrepancies at this point.

We have also found our *Planck* profiles are consistent with the *Planck* results of *Planck* Collaboration et al. (2012V) and *Planck* Collaboration et al (2012X). We interpret this as validating our method of inverting the *Planck* ERCSC data to obtain *Planck* SZ temperature profiles.

In response to a question from a referee, we note the Integrated Sachs-Wolfe (ISW) effect is at most a  $10\mu\text{K}$  effect for clusters/superclusters, (Granett, Neyrinck, & Szapudi 2008). This is too marginal to affect the profiles we recover. The ISW is an even more negligible effect for radio sources, as observed by (Nolta et al. 2004; Sawangwit et al. 2010) where it is shown to be  $\approx 0.3\mu\text{K}$  effect. It is therefore highly unlikely to cause any bias to our results in either the SZ or radio source analyses.

We have also compared our results to those of

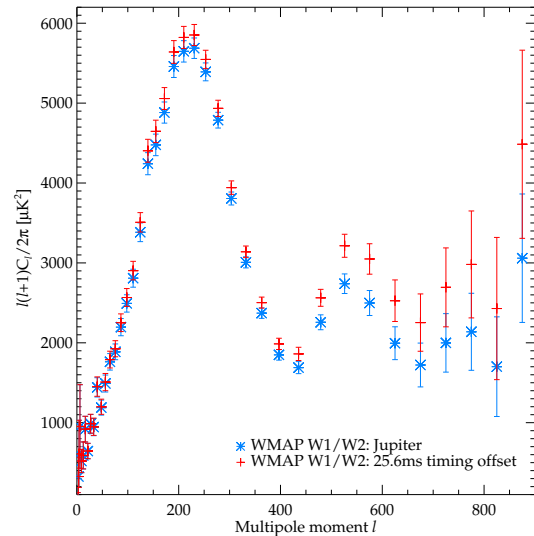


**Figure 15.** The *WMAP* W1/W2  $C_l$  result from debeaming with the Jupiter beam (blue, stars) as compared to the result from debeaming with the timing offset derived beam from Sawangwit (2011) and also shown in Fig. 8 (red, crosses).

Schultz & Huffenberger (2011) whose paper appeared while this one was being refereed. We compare our results directly to theirs in Fig. 14. The *WMAP7* W3 graph they use as an example is significantly wider than any profile shown by Sawangwit & Shanks (2010a) or here. This is because they have used a sample with no cut at all in terms of significance of detection or flux and clearly these data will be strongly affected by Eddington bias. We repeat that at the flux limits used here, the simulations show no sign of such bias and so we are confident that this criticism does not apply to our results. We note that there are additional quality cuts that Schultz & Huffenberger (2011) have made with respect to our work, such as an expanded mask and a culling of close pairs. However, we find that our results are unchanged when we apply them as well. We find that their *WMAP7*-CMBfree and NVSS beam profiles are very comparable to ours for the W3 band and they are wider than the Jupiter profile as can be seen. Schultz & Huffenberger (2011) suggest that the *WMAP7*-CMBfree profiles are wider due to errors on the radio source positions. However, their assumed positional errors may be overestimates for their stacked radio source profiles since the stacks are weighted towards the brighter radio sources which have more accurate positions. The fact that we are using 5GHz GB6 and PMN positions accurate to sub- $0.5$  accuracy in the *WMAP* case and obtain *WMAP7*-CMBfree profiles consistent with Schultz & Huffenberger (2011) suggests that positional errors cannot be the explanation. The main difference with the NVSS results of Schultz & Huffenberger (2011) is their larger errors. Our NVSS sample is  $\approx 4x$  larger than theirs due to our 1.4GHz flux limit of 1Jy compared to their 2Jy limit, this (as well as our larger binning) explains most of the difference in errors. Otherwise the results appear entirely consistent.

We finally show in Fig. 15 the effect wide *Planck* radio source profiles (see Fig. 3f) has on the *WMAP* W1/W2

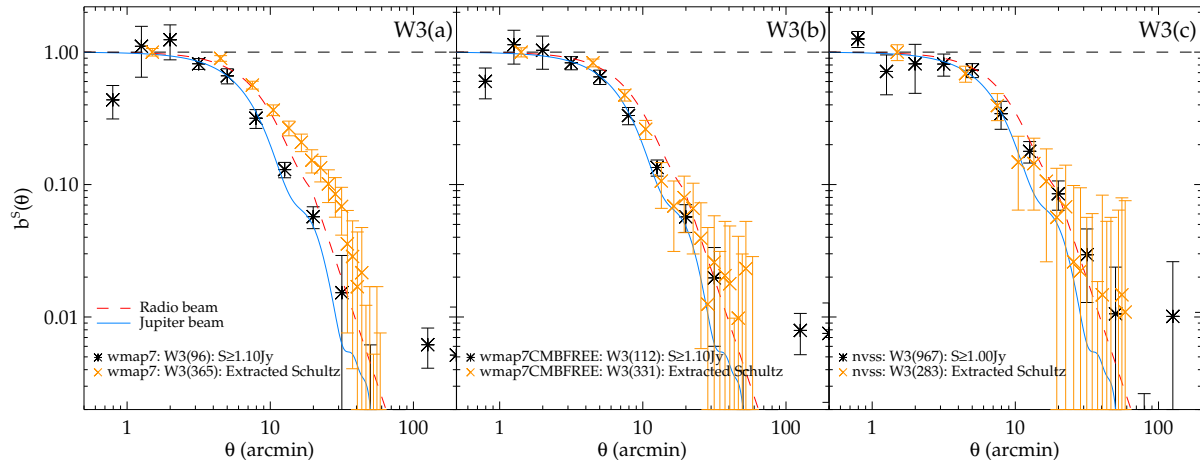


**Figure 14.** (a),(b),(c): The photometrically subtracted stacked *WMAP7* W3  $b^s(\theta)$  profiles for *WMAP7*, *WMAP7* CMB-free and NVSS catalogues as compared to the corresponding W3 results from Schultz & Huffenberger (2011) as taken from their Fig. 5. Also shown are the  $b^s(\theta)$  for the Jupiter beam (blue, solid) and the radio source fit (red, dashed) of Sawangwit & Shanks (2010a).

$C_l$ . We take here the model with the 25.6ms timing offset that gave a reasonable fit to the data in Fig. 8. Otherwise without the model, we would need to extrapolate a fit out to large angles. Then debeaming the raw W1/W2  $C_l$  from PolSpice (Szapudi, Prunet, & Colombi 2001) via eq.(1,2) of Sawangwit & Shanks (2010a), we see that the  $C_l$  shows a modest increase in amplitude at  $\ell < 400$ , with a larger increase at  $\ell > 400$ . This reflects where the Jupiter and timing offset beam are different. At  $\ell < 400$  there is very little difference between the Jupiter and the timing offset beam. We note that this region is essentially unconstrained by the radio source profiles. So the lack of change to the first acoustic peak is tied to the specific details of the timing offset model. A different model could give significantly different results and therefore *WMAP7* first acoustic peak's amplitude and position relies heavily on the accuracy of the observed Jupiter beam beyond  $30'$  scales, which is untested by our observations.

## 11 CONCLUSIONS

We have investigated the beam profile of *WMAP* by comparing beam profiles from radio sources with the Jupiter beam profile. We have compared sources from *Planck*, *WMAP*, *WMAP* CMB-free and NVSS catalogues. We find that in all cases the radio sources show wider profiles than the Jupiter beam with little indication of Eddington bias or dependence on the method of normalisation. Applying our cross-correlation to realistic simulations strongly supports the accuracy of our beam profile measurements. However, it must be said that in the *WMAP7* data the W radio source profiles are less wide than previously found by Sawangwit & Shanks (2010a) in the *WMAP5* release. The rejection of the Jupiter beam is now only  $\approx 3\sigma$  in the *Planck* radio source comparison. But the rejection of the Jupiter beam is reasonably consistent between the admittedly overlapping radio source samples from *Planck*, *WMAP* and NVSS. We have therefore considered explanations for the wide profiles assuming that

they are not statistical fluctuations. Two such possibilities are a non-linearity in the *WMAP* temperature scale and a timing offset in the *WMAP* scan pattern as discussed by Liu & Li (2011). The narrower profiles measured here compared to the Sawangwit & Shanks (2010a) *WMAP5* profiles increase the possibility of their being explained by a timing offset.

We have also found discrepancies between *WMAP* fluxes compared to *Planck* and ground-based fluxes. For  $S < 30\text{Jy}$  the *WMAP* fluxes look to have a non-linear relation with *Planck* fluxes. However, when the further very bright sources discussed by Weiland et al. (2011) with ground-based and *Planck* measurements are included then this flux-flux discrepancy appears more like a linear than a non-linear offset.

We have compared stacked *WMAP* SZ decrements with those measured by *Planck* and by ground-based observations. In contrast to previous reports we now find *WMAP* agrees with both the *Planck* and ground-based data. However this work is not at high enough S/N to distinguish between the timing offset beam of Sawangwit (2011) and the *WMAP* Jupiter beam.

We have shown that transforming the Jupiter beam using a model that fits the radio source profiles results in small but significant changes to the *WMAP*  $C_l$ . At the least, a wider beam would imply a much larger uncertainty in the normalisation and hence the estimate of  $\sigma_8$  from *WMAP*. Unfortunately, faint radio sources cannot check the *WMAP* beam at scales larger than  $30'$  and a wider beam at these scales could, in principle, change the position, as well as the normalisation, of even the first acoustic peak. Clearly it is important to continue to test the calibration and beam profile of *WMAP*, particularly in the W band.

## ACKNOWLEDGMENTS

JRW acknowledges financial support from STFC. US acknowledges financial support from the Royal Thai Govern-

ment. We acknowledge the use of data from NASA *WMAP* and ESA *Planck* collaborations.

## REFERENCES

- Arnaud M., Pratt G. W., Piffaretti R., Böhringer H., Croston J. H., Pointecouteau E., 2010, *A&A*, 517, A92
- Bailey, M. E., & Sparks, W. B. 1983, *MNRAS*, 204, 53P
- Bennett, C. L., et al. 2003, *ApJS*, 148, 97
- Bennett C. L., et al., 2011, *ApJS*, 192, 17
- Bielby R. M., Shanks T., 2007, *MNRAS*, 382, 1196
- Blake C., Wall J., 2002, *MNRAS*, 337, 993
- Bonamente M., Joy M. K., LaRoque S. J., Carlstrom J. E., Reese E. D., Dawson K. S., 2006, *ApJ*, 647, 25
- Cavaliere A., Fusco-Femiano R., 1976, *A&A*, 49, 137
- Chen X., Wright E. L., 2009, *ApJ*, 694, 222
- Condon, J. J., Cotton, W. D., Greisen, E. W., et al. 1998, *AJ*, 115, 1693
- Cotton, W. D., Mason, B. S., Dicker, S. R., et al. 2009, *ApJ*, 701, 1872
- Eddington A. S., 1913, *MNRAS*, 73, 359
- Gold B., et al., 2011, *ApJS*, 192, 15
- Granett B. R., Neyrinck M. C., Szapudi I., 2008, *ApJ*, 683, L99
- Gregory P. C., Scott W. K., Douglas K., Condon J. J., 1996, *ApJS*, 103, 427
- Griffith M. R., Wright A. E., 1993, *AJ*, 105, 1666
- Hill R. S., et al., 2009, *ApJS*, 180, 246
- Hinshaw, G., Spergel, D. N., Verde, L., et al. 2003, *ApJS*, 148, 135
- Jarosik N., et al., 2003, *ApJS*, 145, 413
- Jarosik N., et al., 2011, *ApJS*, 192, 14
- Kenney, J. D., & Dent, W. A. 1985, *ApJ*, 298, 644
- Komatsu E., et al., 2011, *ApJS*, 192, 18
- Lieu R., Mittaz J. P. D., Zhang S.-N., 2006, *ApJ*, 648, 176
- Limon M., et al., 2008, Wilkinson Microwave Anisotropy Probe (*WMAP*): Five Year Explanatory Supplement, [http://lambda.gsfc.nasa.gov/data/map/doc/MAP\\_supplement.pdf](http://lambda.gsfc.nasa.gov/data/map/doc/MAP_supplement.pdf)
- Liu H., Li T.-P., 2011, *ApJ*, 732, 125
- Liszt, H., & Lucas, R. 1999, *A&A*, 347, 258
- Lonsdale, C. J., Doeleman, S. S., & Phillips, R. B. 1998, *AJ*, 116, 8
- Malik, Sawangwit U., Shanks T. & Whitbourn, J.R., 2011, In preparation
- Melin J.-B., Bartlett J. G., Delabrouille J., Arnaud M., Piffaretti R., Pratt G. W., 2011, *A&A*, 525, A139
- Melin J.-B., Bartlett J. G., Delabrouille J., 2006, *A&A*, 459, 341
- Moss A., Scott D., Sigurdson K., 2011, *JCAP*, 1, 1
- Mroczkowski T., et al., 2009, *ApJ*, 694, 1034
- Myers A. D., Shanks T., Outram P. J., Frith W. J., Wolfendale A. W., 2004, *MNRAS*, 347, L67
- Nagai D., Vikhlinin A., Kravtsov A. V., 2007, *ApJ*, 655, 98
- Nolta M. R., et al., 2004, *ApJ*, 608, 10
- Page L., et al., 2003, *ApJS*, 148, 39
- Page L., et al., 2003, *ApJ*, 585, 566
- Piffaretti R., Jetzer P., Kaastra J. S., Tamura T., 2005, *A&A*, 433, 101
- Planck* Collaboration et al, 2011d, The all-sky early Sunyaev-Zeldovich cluster sample, arXiv, arXiv:1101.2024
- Planck* Collaboration et al, 2011f, Statistical analysis of Sunyaev-Zeldovich scaling relations for X-ray galaxy clusters, arXiv, arXiv:1101.2043
- Planck* Collaboration et al, 2011g, Calibration of the local galaxy cluster Sunyaev-Zeldovich scaling relations, arXiv, arXiv:1101.2026
- Planck* Collaboration et al, 2011exp, Explanatory supplement, [http://www.sciops.esa.int/SA/PLANCK/docs/ERCSC\\_Explanatory\\_Supplement.zip](http://www.sciops.esa.int/SA/PLANCK/docs/ERCSC_Explanatory_Supplement.zip)
- Planck* Collaboration et al, 2012V, Pressure profiles of galaxy clusters from the Sunyaev-Zeldovich effect, arXiv, arXiv:1207.4061
- Planck* Collaboration et al, 2012X, Physics of the hot gas in the Coma cluster, arXiv, arXiv:1208.3611
- Pratt G. W., Böhringer H., Croston J. H., Arnaud M., Borgani S., Finoguenov A., Temple R. F., 2007, *A&A*, 461, 71
- Press W. H., Teukolsky S. A., Vetterling W. T., Flannery B. P., 1992, In ‘Numerical Recipes’, CUP:Cambridge, pp. 660
- Refregier A., Spergel D. N., Herbig T., 2000, *ApJ*, 531, 31
- Roukema B. F., 2010, arXiv, arXiv:1007.5307
- Salter, C. J., Reynolds, S. P., Hogg, D. E., Payne, J. M., & Rhodes, P. J. 1989, *ApJ*, 338, 171
- Sawangwit U., Shanks T., 2010a, *MNRAS*, 407, L16
- Sawangwit U., Shanks T., 2010b, In ‘45th Rencontres de Moriond: Cosmology 2010’, Eds Auge, E., Dumarchez, J. & Tran Thanh Van, J., pp. 53-57, GIOI: Vietnam, (arXiv:1006.1270).
- Sawangwit U., Shanks T., Cannon R. D., Croom S. M., Ross N. P., Wake D. A., 2010, *MNRAS*, 402, 2228
- Sawangwit U., 2011, PhD thesis.
- Schultz, K. W., & Huffenberger, K. M. 2011, arXiv:1111.7311
- Shanks T., 1985, *Vistas in Astr.*, 28, 595
- Sunyaev R. A., Zeldovich I. B., 1980, *ARA&A*, 18, 537
- Szapudi I., Prunet S., Colombi S., 2001, *ApJ*, 561, L11
- Tegmark M., de Oliveira-Costa A., 1998, *ApJL*, 500, L83
- Weiland J. L., et al., 2011, *ApJS*, 192, 19
- Wright E. L., et al., 2009, *ApJS*, 180, 283
- Wright, M., & Birkinshaw, M. 1984, *ApJ*, 281, 135
- Wright, M. C. H., & Sault, R. J. 1993, *ApJ*, 402, 546

## APPENDIX A: SZ SELF SIMILAR MODEL

In the self-similar SZ model as employed in the *Planck* ESZ, the fundamental parameters of a cluster are  $P_{500}$ ,  $M_{500}$  and  $R_{500}$ . Using the terminology of Arnaud et al. (2010),

$$M_{500} = \frac{4\pi}{3} R_{500}^3 500 \rho_{crit}, \quad (\text{A1})$$

$$R_{500} = D_a(z) \frac{\theta_{5R_{500}}}{5}. \quad (\text{A2})$$

A  $Y_{500}$  parameter corresponding to these is also defined,

$$Y_{500} = \frac{\sigma_t}{m_e c^2} \frac{4\pi R_{500}^3}{3} P_{500}, \quad (\text{A3})$$

which can be used as a characteristic SZ parameter instead

of  $P_{500}$ . In eq.(A3) the units of  $Y_{500}$  are  $\text{Mpc}^2$ , but are easily convertible to the  $\text{arcmin}^2$  units used in the ESZ and throughout this paper<sup>6</sup>. This  $Y_{500}$  is a distinct quantity from  $Y(R_{500})$  as found by evaluating eq. (9). The introduction of  $Y_{500}$  is well motivated because, as shown by Arnaud et al. (2010), it allows a scale-free description of eq.(9)'s  $Y_{sph}$  and  $Y_{cyl}$  in terms of  $x = R/R_{500}$  as follows,

$$Y_{sph}(x) = Y_{500}I(x), \quad (\text{A4})$$

$$Y_{cyl}(x) = Y_{sph}(5R_{500}) - Y_{500}J(x). \quad (\text{A5})$$

where  $I(x)$  and  $J(x)$  are the spherical and cylindrical scaling functions,

$$I(x) = \int_0^x 3\mathcal{P}(u)u^2 du, \quad (\text{A6})$$

$$J(x) = \int_x^5 3\mathcal{P}(u)(u^2 - x^2)^{1/2} u du. \quad (\text{A7})$$

We therefore find that

$$Y_{cyl}(x) = Y_{500}(I(5) - J(x)). \quad (\text{A8})$$

Finally, we can use the above to calculate  $Y_{cyl}(R)$  and the Compton  $y$  parameter, where  $y(\theta) = \frac{d}{d\Omega} Y_{cyl}(\theta)$ . We now describe three methods for doing so.

**1. Using  $Y(5R_{500})$  as an amplitude:** Since  $Y_{cyl}(5) = Y_{sph}(5) = I(5)Y_{500}$ , eq.(A8) can be expressed as,

$$Y_{cyl}(R) = Y_{cyl}(5R_{500}) \left( 1 - \frac{J(x)}{I(5)} \right). \quad (\text{A9})$$

This is the method we adopt in this paper, it is dependent on both  $Y(5R_{500})$  and  $\theta_{5R_{500}}$ .

**2. Using  $Y_{500}$  as an amplitude:**  $Y_{500}$  can be calculated using  $M_{500}$  and  $P_{500}$ . We can therefore directly evaluate  $Y_{cyl}(R)$  using eq.(A8). This method is independent of the *Planck* provided  $Y(5R_{500})$  and instead solely uses  $\theta_{5R_{500}}$ .

**3. Avoiding the integrated SZ signal:** The Compton  $y$ -parameter can be expressed as (*Planck* Collaboration et al. 2012V),

$$y(r) = \frac{\sigma_t}{m_e c^2} \int_r^{R_{tot}} \frac{2P(r')r' dr'}{(r'^2 - r^2)^{1/2}}. \quad (\text{A10})$$

We can therefore directly evaluate the Compton  $y$ -parameter if a self-similar cluster profile is assumed for  $P(r)$ . This method is independent of the *Planck* provided  $Y(5R_{500})$  and instead solely uses  $\theta_{5R_{500}}$ .

This paper has been typeset from a  $\text{T}_{\text{E}}\text{X}/\text{L}^{\text{A}}\text{T}_{\text{E}}\text{X}$  file prepared by the author.

<sup>6</sup>  $Y[\text{Mpc}^2] = \frac{1}{60^2} \left( \frac{\pi}{180} \right)^2 (D_a[\text{Mpc}])^2 Y[\text{arcmin}^2]$ .